International Journal of Solids and Structures 185–186 (2020) 240–256

Contents lists available at ScienceDirect

International Journal of Solids and Structures

journal homepage: www.elsevier.com/locate/ijsolstr

Theoretical and experimental investigation of performance characteristics and design aspects of cross-spring pivots

L.A. Gonçalves Junior[a,*], R. Theska[b], H.A. Lepikson[c], A.S. Ribeiro Junior[d], S. Linß[e], P. Gräser[b]

[a] Area of Product Development, SENAI CIMATEC, Salvador, BA 41650-010, Brazil
[b] Institute of Design and Precision Engineering, Technische Universität Ilmenau, Ilmenau TH 98693, Germany
[c] SENAI Innovation Institute for Automation, SENAI CIMATEC, Salvador, BA 41650-010, Brazil
[d] Department of Construction and Structures, Universidade Federal da Bahia, Salvador, BA 40210-630, Brazil
[e] Compliant Systems Group, Technische Universität Ilmenau, Ilmenau, TH 98693, Germany

ARTICLE INFO

Article history:
Received 14 February 2019
Revised 13 August 2019
Accepted 15 August 2019
Available online 16 August 2019

Keywords:
Cross-spring pivot
Analytical modeling
Anticlastic curvature
Finite element analysis
Experimental investigation

ABSTRACT

Cross-spring pivots have been widely employed over the last decades in a broad variety of precision engineering applications due to the high motion repeatability achieved thanks to the absence of stick slip and clearance. In this paper, the non-linear effect of the anticlastic curvature of the leaf-springs is considered for the accurate analytical modeling of the elasto-kinematic behavior of cross-spring pivots. Finite element analyses (FEA), based on a non-linear thin-shell model, are carried out in order to compare them with the analytical results for the main performance parameters of this type of device, i.e. center-shift, rotational stiffness and stress in the leaf-springs. Furthermore, an experimental setup is built to assess the applicability limits of both models. Finally, remarkable performance aspects of cross-spring pivots are discussed aiming for design improvements.

1. Introduction

Flexural joints are constructional elements designed to accomplish rotational motion through bending-based elastic deflection of their own. They are characterized by a high "in-plane" rotational compliance and a high stiffness in transverse directions. Furthermore, they provide a variety of advantages over conventional sliding and rolling joints, such as: no friction (just internal bonding forces), no clearance, absence of stick slip, low wear and no need for maintenance (Wittrick, 1948; Lobontiu and Garcia, 2003; Tian et al., 2010; Bitencourt et al., 2015; Gómez et al., 2015; Merriam et al., 2016; Marković and Zelenika, 2017; Hongzhe and Shusheng, 2010a; Meng et al., 2014). Due to these attributes, flexural joints are preferentially employed in several applications of precision engineering, aerospace fields, MEMS, positioning and manipulation systems, in metrology (weighing-machines, dynamometers, seismometers and pressure transducers), optical instrumentation and gyroscopes (Wittrick, 1948; Zelenika and Bona, 2002; Gonçalves Jr., 2016; Bi et al., 2012; Yong et al., 2008), i.e. in applications that usually require a high repeatability of motion in limited angles of rotation.

In order to fulfill the requirements of different applications, several types of primitive and complex flexural joints have been exploited. Primitive flexural joints are commonly classified in the literature as notch and leaf-type flexure hinges (Pei et al., 2009; 2010). Notch-type flexure hinges are characterized by a markedly high stiffness in transversal direction. On the other hand, a strongly limited rotation capability due to stress concentration and an "in-plane" parasitic deviation of its rotational center arise as their major drawbacks (Bi et al., 2012; Pei et al., 2010; Linß et al., 2011; 2017; Liu et al., 2014). Nevertheless, the rotational range can be enlarged by the utilization of leaf-type hinges which are able to accomplish a larger stroke of motion, in expense, however, of an even higher center-shift.

In face of the limitations presented by the primitive flexural joints, special attention has been given in the recent years to the design of more complex flexural joints, commonly obtained by the combination of two or more modules of primitive joints. Within the group of these joints, many examples can be mentioned. The cartwheel hinge (Pei et al., 2009; Choi et al., 2007) which is

* Corresponding author.
E-mail address: luis.antonio@fieb.org.br (L.A. Gonçalves Junior).

https://doi.org/10.1016/j.ijsolstr.2019.08.023

Nomenclature

A, x, b	coefficient matrix, vector of unknowns (i.e. center of rotation coordinates) and vector of constant terms of the linear system employed for the calculation of the cross-spring pivot center-shift
a_j, b_n, c_j	Coefficients of polynomials employed to support the design of cross-spring pivots, with $j = 0, \ldots, 9$ and $n = 0, \ldots, 8$
D	cross-spring pivot center-shift
d, d_{FEM}, d_{exp}	normalized analytical, FEM and experimental center-shifts
D_{OX}, D_{OY}	optical path error due to the rotation of the corner cube reflectors
DX, DY	components of the cross-spring pivot center-shift
dx, dy	normalized components of the cross-spring pivot center-shift
E	material Young's modulus
EI_i, $(EI_i)^*$	initial and actual flexural rigidity of the ith leaf-spring
I	second moment of area of the leaf-spring cross section
k, k_{FEM}, k_{exp}	normalized analytical, FEM and experimental cross-spring pivot rotational stiffness
L	leaf-spring length
L_{12}	length of the cross-spring pivot moving member
M, F, P	couple, horizontal and vertical forces acting on the cross-spring pivot moving member
m, f, p	normalized couple, horizontal and vertical forces acting on the cross-spring pivot moving member
$m_i(x_i)$	normalized internal bending moment along the ith leaf-spring
M_i, F_i, P_i	couple, transverse and normal forces acting on the moving edge of the ith leaf-spring
m_i, f_i, p_i	normalized couple, transverse and normal forces acting on the moving edge of the ith leaf-spring
m_i^*, f_i^*, p_i^*	normalized couple, transverse and normal forces acting on the moving edge of the ith leaf-spring multiplied by the corrective factor ξ_i
OXY_i, OXY	local coordinate system of the ith leaf-spring and global coordinate system
R	principal curvature radius of an arbitrary leaf-spring
$R_i(X_i)$, $\overline{R_i}$	variable and mean principal curvature radii of the ith leaf-spring
s, c	non-dimensional parameters
S_U	material ultimate strength
T	leaf-spring thickness
v_1, v_2	displacements of nodes 1 and 2 in Y-direction
W	leaf-spring width
x_c, y_c	normalized coordinates of the cross-spring pivot center of rotation.
X_i, Y_i	coordinates of the ith leaf-spring in the local coordinate system OXY_i
x_i, y_i	normalized coordinates of the ith leaf-spring in the local coordinate system OXY_i
y_s	normalized cross section Y coordinate from the neutral axis

Greek letters

α	semi-angle between the leaf-springs
β_i	Searlo's parameter related to ith leaf-spring
Δd	difference of the normalized FEM and experimental center-shifts to the analytical results
ΔX_i, ΔY_i	displacement components of the ith leaf-spring moving edge in the local coordinate system OXY_i
δx_i, δy_i	normalized displacement components of the ith leaf-spring moving edge in the local coordinate system OXY_i
λ	non-dimensional parameter which defines the length of the leaf-springs crossing point
μ_r	coefficient of friction of the pulleys
ν	material Poisson's ratio
Φ_i	anticlastic factor related to ith leaf-spring
$\sigma_{0.2}$	material yield strength
σ_1, $\sigma_{1_{exp}}$	analytical and experimental stress in the leaf-spring 1
$\sigma_i(x_i, y_s)$	normal stress along the ith leaf-spring
θ	rotational angle of the cross-spring pivot moving member
$\epsilon_{\text{cor. fact}}$, ϵ_{sys}	convergence tolerances of the corrective factor ξ_i and the non-linear system
ξ_i	corrective factor of the ith leaf-spring flexural rigidity

characterized by a small center-shift but a still limited range of motion due to high stress concentration on its modules. The butterfly configuration proposed by Henein et al. (2003) that provides a diminished center deviation and a large stroke of motion, with the detrimental effect of a high geometric complexity, and the cross-spring pivot which is substantially simpler in terms of geometric arrangement whereas it also allows a high range of rotation (Marković and Zelenika, 2017; Gonçalves Jr., 2016). More recently, studies of cross-spring pivot variations were delivered by Dearden et al. (2018) and Merriam and Howell (2016) in order to obtain hollow-shaft integrated designs and reduced stiffness configurations, respectively.

When cross-spring pivots are considered to be used in high-precision applications, there are some design aspects that shall be observed. For instance, the most commonly found geometric arrangement of cross-spring pivots (Fig. 7(a)), whose leaf-springs are forming a symmetric cross, presents a substantially high center-shift (at least five times higher than the equivalent cartwheel hinge (Hongzhe and Shusheng, 2010a)). On the other hand, asymmetric configurations provide smaller center deviation

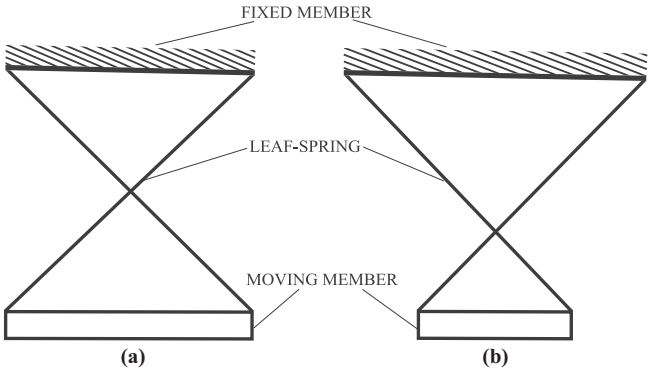

Fig. 1. Cross-spring pivot geometric configurations – (a) symmetric and (b) asymmetric.

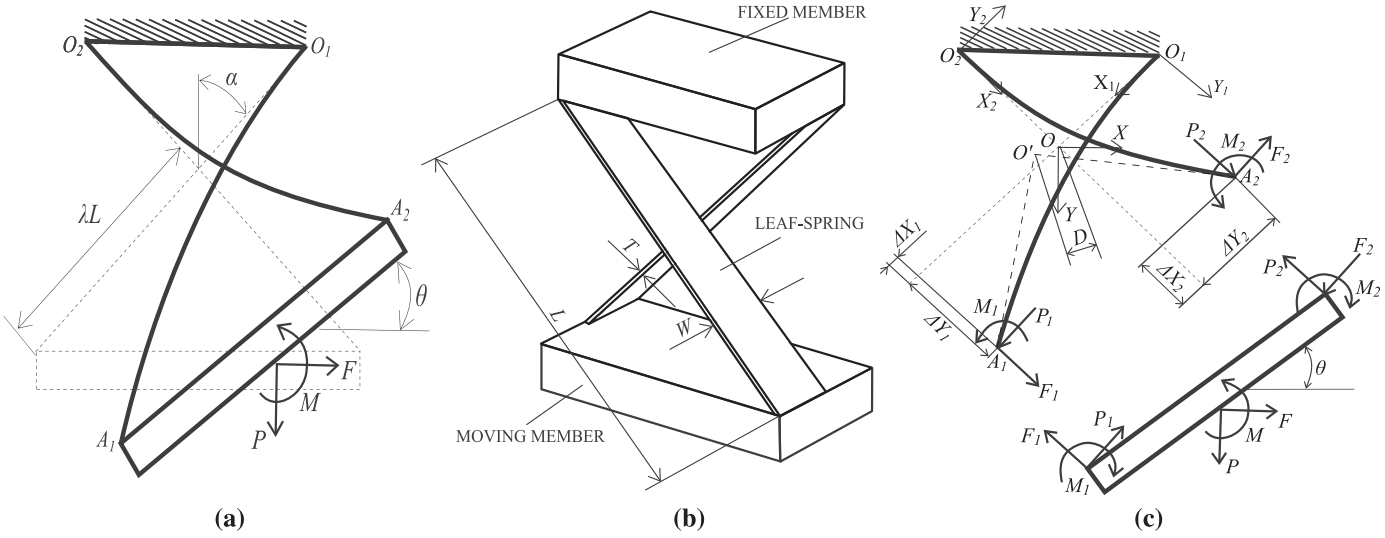

Fig. 2. Cross-spring pivot – (a) geometric parameters, (b) shape parameters and (c) center-shift and load-displacement representation.

accompanied, however, by the detrimental effects of higher "in-plane" stiffness and critical stresses (Fig. 7(b)). Therefore, a suitable modeling of the pivot elasto-kinematic behavior is needed to predict accurately performance characteristics such as the center-shift, rotational stiffness and stress levels in the leaf-springs, as well as to provide useful design insights that enable the choice of the most adequate geometric arrangement for a given application.

Several approaches to model the elasto-kinematic behavior of cross-spring pivots have been investigated by different authors over the last decades. Some are restricted to specific geometric configurations and loading conditions, whereas others are not able to provide design insights. Just a few of them are able to fulfill both, performance prediction and geometric optimization. In this sense, Haringx (1949) proposed a model – based on the solution through elliptic integrals of the exact expression for the leaf-spring curvature – to predict the center-shift of the symmetric pivot loaded by pure couple for even large angles of rotations. Similarly, the approaches based on kinematic considerations (Wuest, 1950) and pseudo-rigid-body method (Pei et al., 2010) are addressed to the determination of this parasitic motion. They are, though, less accurate. In order to overcome the load limitation, Zelenika and Bona (2002) took into account a planar general condition of load (vertical, horizontal and couple) to model the elasto-kinematic behavior of symmetric cross-spring pivots. However, for large rotational angles, this approach presents lower accuracy than the exact solution of Haringx (1949) due to the use of the approximated leaf-spring curvature expression.

Approaches proposed by Hongzhe and Shusheng (2010a,b) provide a geometric parametrization of the pivot submitted to a general "in-plane" loading. Although, these approaches showed to be helpful tools in early design stages, they are derived from the parametric closed-form result presented by Awtar (2004) which is based on approximations (series, linear, inverse linear and inverse quadratic approximations) taken in the solution of the approximated load-displacement equation of the leaf-spring. Therefore, they provide less accuracy in the prediction of the pivot performance parameters when compared with models based on the exact and even the approximated curvature expression of the leaf-spring.

In our previous work Gonçalves Jr. et al. (2014), an analytical model was developed to accomplish both, accurate performance prediction and geometric optimization. In the present work, the pivot rotational stiffening induced by the non-linear effect of the anticlastic curvature reduction for increasing deflections of the leaf-springs is introduced in the analytical model. In addition, a non-linear thin shell-based FEM model is also proposed and an experimental setup, based on laser interferometry, optical systems and extensometry is built. The experimental measurements, together with the reported in the literature, are used to check the limits of applicability of both models. As far as the effectiveness of the analytical model is assured, it is finally employed to discuss design aspects of cross-spring pivots.

2. Improved analytical model

In order to accomplish a geometric optimization, the pivot geometry is firstly parametrized. Thus, the following geometric parameters are defined: $\lambda \in [0,1]$ and $\alpha \in (0, \pi/2)$ which determine the leaf-springs crossing point and the semi-angle between them. In addition, the shape parameters *L, W, T* – length, width and thickness – are used to represent the dimensions of the leaf-springs, as shown in Fig. 2(a) and (b), respectively.

2.1. Load-rotational relationship of the cross-spring pivot

According to Zelenika and Bona (2002), the load-rotational relationship of a cross-spring pivot submitted to a general planar load condition *M, F* and *P* – couple, horizontal and vertical loads – may be described by 11 variables (θ, P_1, P_2, F_1, F_2, M_1, M_2, ΔY_1, ΔY_2, ΔX_1 and ΔX_2), as shown in Fig. 2(c).

For the sake of mathematical convenience, all displacements and lengths are normalized by *L*, forces by EI/L^2 and moments by EI/L as follows (Gonçalves Jr. et al., 2014):

$$m_i = \frac{M_i L}{EI},\ f_i = \frac{F_i L^2}{EI},\ p_i = \frac{P_i L^2}{EI},\ x_i = \frac{X_i}{L},\ y_i = \frac{Y_i}{L},\ \delta x_i = \frac{\Delta X_i}{L},$$

$$\delta y_i = \frac{\Delta Y_i}{L},\ dx = \frac{DX}{L},\ dy = \frac{DY}{L},\ d = \frac{D}{L},\ 1 = \frac{L}{L},\ t = \frac{T}{L},$$

where *E* is the material Young's modulus and *I* the second moment of area of the leaf-spring cross section. The dimensional and the equivalent non-dimensional quantities are, respectively, represented by upper and lower case letters from now on. Moreover, the subscript *i* may be assigned as 1 or 2 and refers either to the two leaf-springs or to the quantities expressed in the corresponding local coordinate system OXY_i. On the other hand, it is suppressed for the quantities written in the global coordinate system *OXY*.

In order to determine all 11 unknowns, a non-linear system of 11 equations is built. In the following, Eqs. (1)–(3) are obtained by the equilibrium conditions of the pivot moving member.

Eqs. (4) and (5), in turn, come up from the geometric compatibility between this member and the moving edges of the leaf-springs in X and Y directions.

$$f = (p_2 - p_1)\sin(\alpha) + (f_1 + f_2)\cos(\alpha), \tag{1}$$

$$p = (p_1 + p_2)\cos(\alpha) + (f_1 - f_2)\sin(\alpha), \tag{2}$$

$$\begin{aligned} m = m_1 + m_2 + [(p_1 - p_2)\cos(\alpha) + (f_1 + f_2)\sin(\alpha)] \\ \times\lambda 1\sin(\alpha)\cos(\theta) - [(p_1 + p_2)\sin(\alpha) - (f_1 - f_2)\cos(\alpha)] \\ \times\lambda 1\sin(\alpha)\sin(\theta), \end{aligned} \tag{3}$$

$$\begin{aligned} (\delta y_1 - \delta y_2)\cos(\alpha) + (\delta x_1 + \delta x_2)\sin(\alpha) \\ = 2\lambda 1\sin(\alpha)(1 - \cos(\theta)), \end{aligned} \tag{4}$$

$$(\delta y_1 + \delta y_2)\sin(\alpha) - (\delta x_1 - \delta x_2)\cos(\alpha) = 2\lambda 1\sin(\alpha)\sin(\theta). \tag{5}$$

The remaining six equations (Eqs. (7), (8) and (10)) are given by the solutions of the approximated curvature expression (for a tip deflection of $0.1L$ the maximum error is in the order of 3.4% Awtar, 2004), the elastic stretching and kinematic constraint (constant arc length) of the deformed leaf-spring shown in Fig. 3.

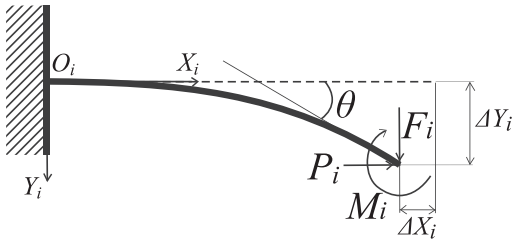

Fig. 3. Load-displacement representation of the leaf-spring.

$$\delta y_i \approx \xi_i f_i \left[\frac{\sqrt{\xi_i p_i} - \tanh\left(\sqrt{\xi_i p_i}\right)}{(\xi_i p_i)^{(3/2)}}\right] + \xi_i m_i \left[\frac{\cosh\left(\sqrt{\xi_i p_i}\right) - 1}{\xi_i p_i \cosh\left(\sqrt{\xi_i p_i}\right)}\right]. \tag{8}$$

The elastic stretching and kinematic constraint of the leaf-spring, in turn, may be written as follows (Gonçalves Jr. et al., 2014):

$$\delta x_i \approx -\frac{p_i}{s} + \frac{1}{2}\int_0^1 \left[\frac{\mathrm{d}}{\mathrm{d}x_i} y(x_i)\right]^2 \mathrm{d}x_i. \tag{9}$$

Finally, substituting Eq. (A.1) in Eq. (9) and performing the integration results in:

$$\begin{aligned} \delta x_i \approx & -\frac{p_i}{s} \\ & + (\xi_i f_i)^2 \left[\frac{10\sqrt{\xi_i p_i}\cosh\left(\sqrt{\xi_i p_i}\right) + 2\sqrt{p_i}\cosh\left(3\sqrt{\xi_i p_i}\right) - 3\sinh\left(\sqrt{\xi_i p_i}\right) - 3\sinh\left(3\sqrt{\xi_i p_i}\right)}{4(\xi_i p_i)^{(5/2)}\cosh\left(3\sqrt{\xi_i p_i}\right) + 12(\xi_i p_i)^{(5/2)}\cosh\left(\sqrt{\xi_i p_i}\right)}\right] \\ & + {\xi_i}^2 f_i m_i \left[\frac{3\cosh\left(\sqrt{\xi_i p_i}\right) - 2\cosh\left(2\sqrt{\xi_i p_i}\right) + \cosh\left(3\sqrt{\xi_i p_i}\right) - \sqrt{\xi_i p_i}\sinh\left(2\sqrt{\xi_i p_i}\right) - 2}{(\xi_i p_i)^2\cosh\left(3\sqrt{\xi_i p_i}\right) + 3(\xi_i p_i)^2\cosh\left(\sqrt{\xi_i p_i}\right)}\right] \\ & + (\xi_i m_i)^2 \left[\frac{\sinh\left(\sqrt{\xi_i p_i}\right) + \sinh\left(3\sqrt{\xi_i p_i}\right) - 4\sqrt{\xi_i p_i}\cosh\left(\sqrt{\xi_i p_i}\right)}{4(\xi_i p_i)^{(3/2)}\cosh\left(3\sqrt{\xi_i p_i}\right) + 12(\xi_i p_i)^{(3/2)}\cosh\left(\sqrt{\xi_i p_i}\right)}\right], \end{aligned} \tag{10}$$

The well-known expression of the approximated curvature may be expressed in the non-dimensional form as follows (Awtar, 2004):

$$\frac{\mathrm{d}^2}{\mathrm{d}x_i^2} y_i(x_i) = -p_i^*(\delta y_i - y_i(x_i)) + f_i^*(1 - x_i) + m_i^*, \tag{6}$$

where $p_i^* = \xi_i p_i$, $f_i^* = \xi_i f_i$ and $m_i^* = \xi_i m_i$. ξ_i is a corrective factor defined by the ratio between the initial and actual flexural rigidity of the leaf-spring (EI and $(EI)_i^*$, respectively). This factor takes into account the non-linear effect of the leaf-spring stiffening induced by the anticlastic curvature reduction in increasing the deflections. A detailed discussion about this effect is presented in the next section.

The right hand side of Eq. (6) represents the normalized internal bending moment $m_i(x_i)$ along the leaf-springs multiplied by ξ_i.

Eq. (6) can be solved by double integration and the use of proper boundary conditions, as shown in Appendix A. Thus, the leaf-spring slope and transverse deflection at the moving edge are obtained assigning $x_i = 1$ in Eqs. (A.1) and (A.2) as follows (Gonçalves Jr. et al., 2014):

$$\theta \approx \xi_i f_i \left[\frac{\cosh\left(\sqrt{\xi_i p_i}\right) - 1}{\xi_i p_i \cosh\left(\sqrt{\xi_i p_i}\right)}\right] + \frac{\xi_i m_i \tanh\left(\sqrt{\xi_i p_i}\right)}{\sqrt{\xi_i p_i}}, \tag{7}$$

where $s = 12(\frac{L}{T})^2 = \frac{12}{t^2}$.

2.2. Anticlastic curvature

According to the classic bending theory, a narrow leaf-spring ($W/T << 1$) undergoes a plane stress state when a pure couple is applied to it. In this case, its flexural rigidity is given by EI and, due to Poisson's effect, an anticlastic curvature (in transverse direction) $-\nu/R$ occurs (where $-\nu$ is the Poisson's ratio and R the principal curvature radius). On the other hand, when an unconstrained wide leaf-spring ($W/T >> 1$) is bent by a pure couple, it remains fairly flat in transverse direction, with exception of the boundary regions. Therefore a plane strain state is developed and the flexural rigidity becomes $EI/(1 - \nu^2)$ (Fung and Wittrick, 1955; Pomeroy, 1970). In a transition state, however, the anticlastic curvature is partially developed and the flexural rigidity depends no longer only on the ratio W/T, but also on the principal curvature radius R (Wang et al., 2005). Thus, for general cases, the flexural rigidity may be approached with an accuracy of better than 1% by the following non-linear equation (Pomeroy, 1968):

$$(EI)_i^* = \frac{EI}{(1 - \phi_i\nu^2)}. \tag{11}$$

The parameter Φ_i in Eq. (11) is an anticlastic factor (non-dimensional number). This factor may be expressed as stated by

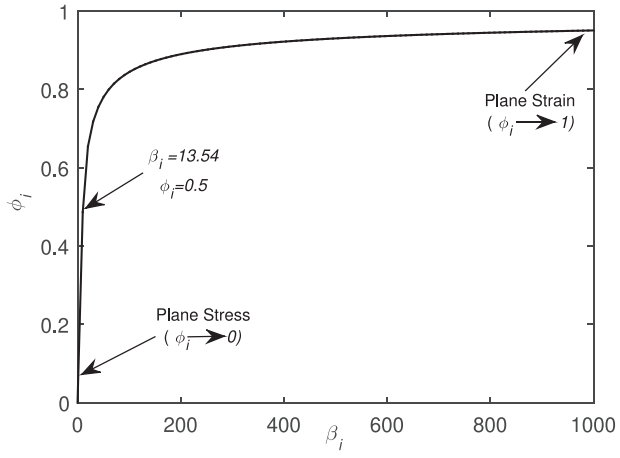

Fig. 4. Anticlastic factor Φ_i as function of the Searle's parameter β_i.

Pomeroy (1970):

$$\phi_i = 1 - \frac{2}{c\sqrt{\beta_i}}\left(\frac{\cosh c\sqrt{\beta_i} - \cos c\sqrt{\beta_i}}{\sinh c\sqrt{\beta_i} + \sin c\sqrt{\beta_i}}\right), \tag{12}$$

where the Searle's parameter $\beta_i = W^2/R_i t$ is the non-dimensional factor defined in Searle (1908) and $c = \sqrt[4]{3(1-\nu^2)}$ is also a non-dimensional number which depends only on the material Poisson's ratio.

Fig. 4 shows that Φ_i tends to 0 when $\beta_i << 1$ and increases asymptotically to 1 for $\beta_i >> 1$ so that, at the limits, Eq. (9) also holds the leaf-spring plane stress and plane strain cases.

For a given angle θ of rotation of the pivot moving member, the curvature $1/R_i(X_i)$ is not constant along the leaf-spring. However, for just smooth variations, Eqs. (11) and (12) may still be used (Meijaard, 2011). In this case, in order to calculate β_i, a mean value of the leaf-spring curvature (reciprocal of the curvature radius) is taken (Pomeroy, 1968):

$$\frac{1}{\overline{R_i}} = \frac{1}{L}\int_0^L \frac{1}{R_i(X_i)}\mathrm{d}X_i. \tag{13}$$

Eq. (13) may be written in terms of the normalized internal bending moment as follows:

$$\begin{aligned}\frac{1}{\overline{R_i}} &= \int_0^1 \frac{1}{L}\xi_i m_i(x_i)\mathrm{d}x_i \\ &= \frac{1}{L}\int_0^1 [-p_i^*(\delta y_i - y_i(x_i)) + f_i^*(1-x_i) + m_i^*]\mathrm{d}x_i.\end{aligned} \tag{14}$$

Thus, substituting Eq. (A.2) into Eq. (14) and performing the integration, a closed-form expression for the mean curvature is obtained:

$$\begin{aligned}\frac{1}{\overline{R_i}} = &-\frac{\delta y_i p_i\sqrt{\xi_i p_i}\sinh\sqrt{\xi_i p_i} - m_i\sqrt{\xi_i p_i}\sinh\sqrt{\xi_i p_i}}{p_i L} \\ &+\frac{f_i(1-\cosh\sqrt{\xi_i p_i} + \sqrt{\xi_i p_i}\sinh\sqrt{\xi_i p_i})}{p_i L}\end{aligned} \tag{15}$$

Fig. 5 shows the calculation procedure of the elasto-kinematic behavior of cross-spring pivots. At this point, it is important to emphasize that two interactive procedures are performed in order to obtain the final solution of the load-displacement relationship block (11 unknowns presented in the beginning of this section): one for the non-linear system defined by Eqs. (1)–(5), (7), (8) and (10) and another for the calculation of the corrective factor ξ_i. The Levenberg-Marquardt algorithm proved to be efficient in solving medium-size problems and therefore is employed to solve the non-linear system (Gonçalves Jr. et al., 2014; Roweis, 2018). The corrective factor ξ_i calculation, in turn, is carried out by means of simple iterations. Performed tests showed, in this case, that the final solution for ξ_i is reached in a maximum of three iterations, when a convergence tolerance $\epsilon_{\text{cor. fact}} = 0.001$ is considered.

Another non-linear effect that occurs as a consequence of the moving member rotation is the additional rotational stiffening of the pivot induced by the anticlastic curvature preclusion at the ends of the leaf-springs due to the clamping constraints (Brouwer et al., 2013). According to Meijaard (2011) the non-dimensional factor L/W may be used as a measure of the influence of this effect on the leaf-spring rigidity. In this sense, the smaller the ratio L/W, the greater is the additional stiffening induced by the clamped edges of the leaf-springs. Furthermore, this effect is even more relevant when the leaf-springs undergo substantially small displacements (tip deflections smaller than $0.01L$). In fact, the additional rotational stiffening of the pivot is dominated by small ratios of L/W ($L/W < 4$) for very small deflections of the leaf-springs (i.e. very small rotations of the moving member) whereas it turns into being governed by the anticlastic curvature reduction (large Searlo's parameter, $\beta_i > 10$) in the rest of the pivot rotational range (Brouwer et al., 2013). Since the clamping constraint effect is relevant under restrict conditions ($L/W < 4$ and very small deflections of the leaf-springs) and due to the mathematical complexity to incorporate it into the analytical model, it is hereby neglected.

2.3. Performance parameters

The solution of the load-displacement block allows the calculation of the cross-spring pivot performance parameters (center-shift, rotational stiffness and stress in the leaf-springs), as discussed below.

2.3.1. Center-shift

The cross-spring pivot center-shift $\overline{OO'}$ is inherent to the rotational motion of this flexural joint, as shown in Fig. 2(c). This parasitic motion may be determined by the geometric consideration in which the intersection of the straight lines tangent to the leaf-springs at the moving edges (points A_1 and A_2) defines the position of the pivot center of rotation, for a given rotational angle θ of its moving member.

The normalized equations of each straight line tangent at A_1 and A_2 may be written in the local leaf-spring coordinate systems OXY_i as follows (Hasselmeier, 1951):

$$y_i - \delta y_i = \tan(\theta)[x_i - (1 - \delta x_i)]. \tag{16}$$

To determine the intersection point, the linear system composed by both straight lines must be solved. Therefore, they need to be written at the same coordinate system. Thus, performing a rotation and a translatory transformation from the local coordinate systems OXY_i to the global coordinate system OXY results in:

$$\mathbf{A}\mathbf{x} = \mathbf{b}, \tag{17}$$

where:

$$\mathbf{A} = \begin{bmatrix} \cos(\alpha) + \sin(\alpha)\tan(\theta) & \sin(\alpha) - \cos(\alpha)\tan(\theta) \\ \cos(\alpha) - \sin(\alpha)\tan(\theta) & -\sin(\alpha) - \cos(\alpha)\tan(\theta) \end{bmatrix},$$

$$\mathbf{x} = \begin{Bmatrix} x_c \\ y_c \end{Bmatrix}, \quad \mathbf{b} = \begin{Bmatrix} (\delta x_1 - \lambda)\tan\theta + \delta y_1 \\ (\delta x_2 - \lambda)\tan\theta + \delta y_2 \end{Bmatrix}.$$

Finally, the normalized center-shift is determined by:

$$d = \sqrt{dx^2 + dy^2} = \sqrt{{x_c}^2 + {y_c}^2}, \tag{18}$$

where x_c, y_c are the normalized coordinates of the pivot center of rotation.

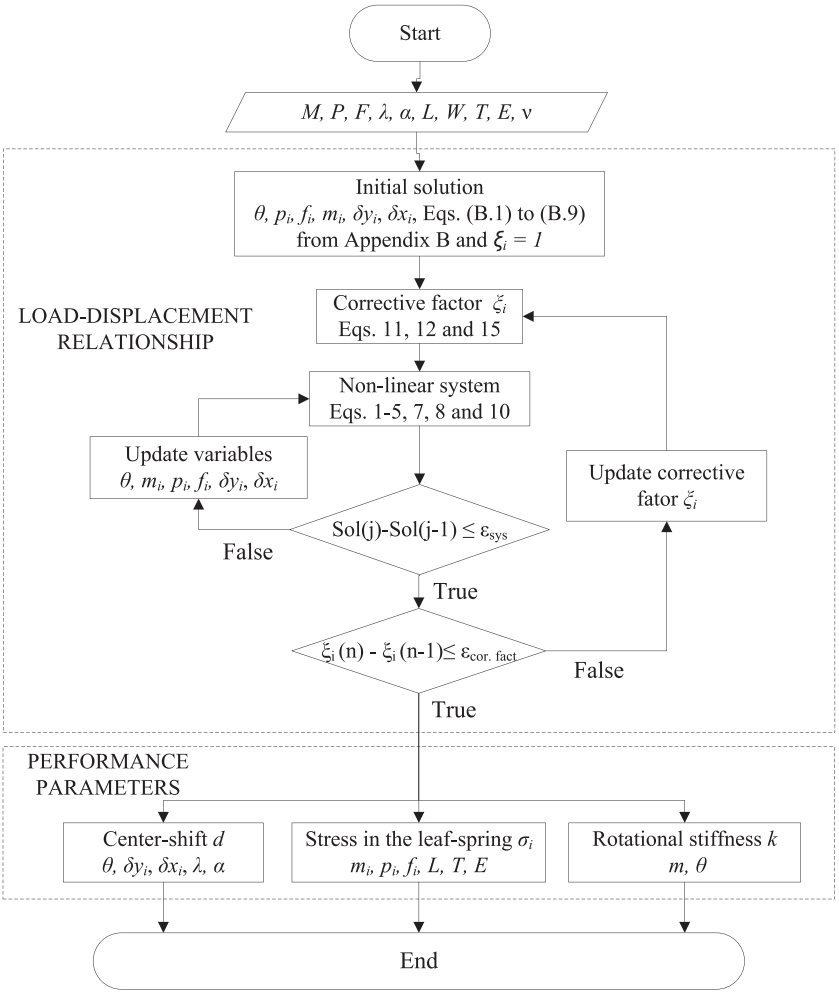

Fig. 5. Flowchart of the calculation procedure of the elasto-kinematic behavior of cross-spring pivots.

2.3.2. Rotational stiffness

The cross-spring pivot rotational stiffness provides a measure of the angular response of this flexural joint to a certain loading applied to its moving member. In addition, this parameter is useful to evaluate the pivot stability, since it reveals at which load conditions the buckling of the leaf-springs occurs, i.e., when it becomes negative. The normalized rotational stiffness may be readily defined by Gonçalves Jr. et al. (2014):

$$k = \frac{m}{\theta}, \tag{19}$$

where m is the normalized couple applied to the pivot moving member.

2.3.3. Stress analysis

The analysis of stress developed along the leaf-springs is useful to determine the motion capability of the cross-spring pivot, once it is designed to work within the elastic range (under the material yield strength).

Knowing that the leaf-springs are considered to be slender ($L/T >> 1$), the shear stress may be neglected. Thus, the stress distribution along them may be expressed as follows (Hongzhe and Shusheng, 2010b):

$$\sigma_i(x_i, y_s) = -\frac{\sqrt{3}Em_i(x_i)y_s}{\sqrt{s}} + \frac{Ep_i}{s}, \tag{20}$$

where the first term on right side of Eq. (20) represents the bending stress and the second expresses the axial stress. In addition, $y_s \in [-1, 1]$ is the stress evaluation point on the leaf-spring cross section (from the neutral axis) normalized by the half of the thickness $T/2$.

3. FEM model

In order to verify the analytical results reported in the literature, models based on non-linear beam finite elements have been widely proposed so far (Merriam et al., 2016; Marković and Zelenika, 2017; Hongzhe and Shusheng, 2010a; Bi et al., 2012; Merriam and Howell, 2016; Hongzhe and Shusheng, 2010b; Gonçalves Jr. et al., 2014). In this paper, however, to properly capture the transition between the plane stress and plane strain states, a more comprehensive model based on non-linear thin shell elements was built in the environment of the well-known commercial package ANSYS™. For this purpose, the element "SHELL63" was used. This element has four-nodes and six degree of freedom (DOFs) on each node: translation along and rotation about *X*, *Y* and *Z* axes. Both bending and membrane stiffness are permitted. In addition, large deflections and stress stiffening are also included on its formulation (ANSYS, 2007).

Owing to the capabilities aforementioned, the element "SHELL63" is able to adequately represent the non-linear effects of the pivot kinematics and the rotational stiffening induced by the leaf-spring anticlastic curving reduction (Brouwer et al., 2013). On the other hand, to take into account the anticlastic curvature preclusion due to the clamping constraints, suitable

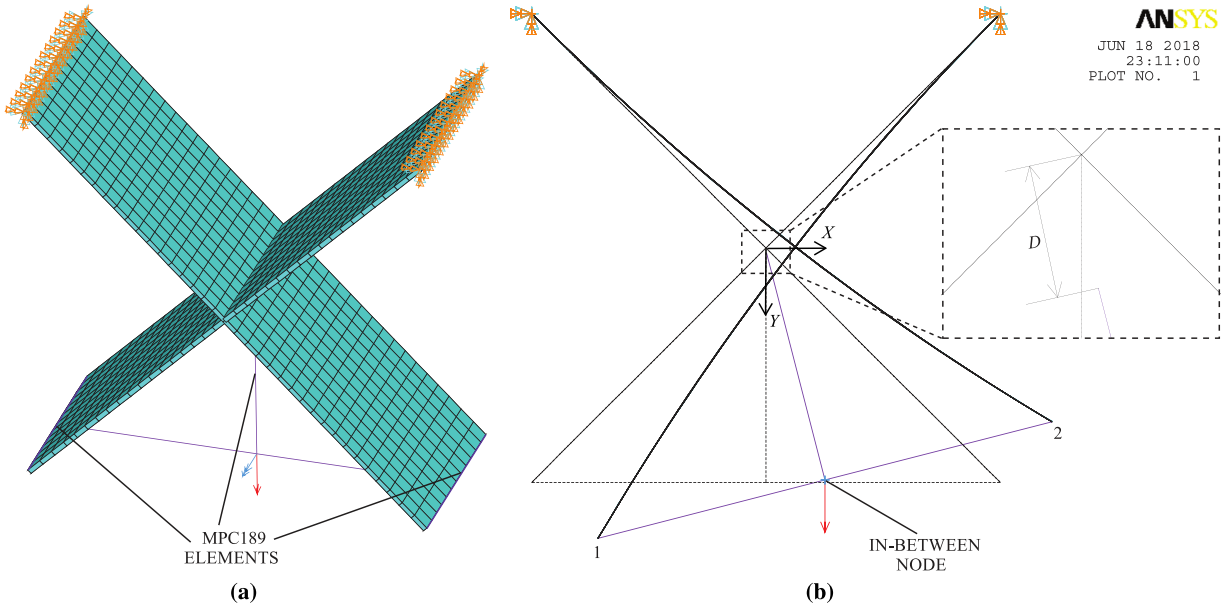

Fig. 6. FEM idealization – (a) loading and mesh discretization and (b) center-shift.

boundary conditions have to be used. In this case, all six DOFs of the nodes at the fixed member are constrained, whereas rigid elements with six DOFs (beam-like "MPC189" elements) are used along-width to prevent the transverse curvature development on the moving edges, as shown in Fig. 6(a).

The compatibility of motion between the moving edges is also assured by two "MPC189" elements. They both, in turn, play the role of the pivot moving member. The in-between node is used as a load and couple application point. Furthermore, another element of the same type is vertically placed from this node up to the crossing point of the undeformed leaf-springs, in order to capture the position of the pivot center of rotation for a given rotational angle θ of the moving member, as shown in Fig. 6(b). This rotational angle, in turn, is given by:

$$\theta = \arcsin\left(\frac{|v_1 - v_2|}{L_{12}}\right), \tag{21}$$

where v_1 and v_2 represent the displacement of nodes 1 and 2 in Y direction and L_{12} the moving member length (Fig. 6(b)). In addition, a typical isotropic linear elastic material model was employed ($E = 200\,\text{GPa}$, $\nu = 0.3$).

Convergence tests revealed that, for any "in-plane" loading condition, 12 elements along the width provide accurate results (difference smaller than 0.1% to a further refinement with 16 elements) for the stress in the leaf-springs, rotational angle θ and center-shift of the pivot. Thus, in order to obtain a mesh with good quality a mapped discretization with a maximum aspect ratio of 1.12 was created so that 36 elements were fitted along the length for a 20-mm-width per 60-mm-long leaf-spring configuration (the same leaf-spring dimensions are used in the experimental prototypes). In order to simulate the cross-spring pivot behavior properly, no nodal connectivity at the intersection line of the leaf-springs was established. Moreover, the gravity effect was not considered, since a self-weight compensation was applied in the experimental tests. Finally, a solution control of static large displacement was chosen to perform the calculations.

4. Experimental procedure

Experimental tests were carried out to check the effectiveness and limits of applicability of the improved analytical model. Thus, in the following the cross-spring pivot design and the experimental approach applied in the tests are described.

4.1. Design of the cross-spring pivots

Two cross-spring pivot configurations were set up with crossing points defined by $\lambda = 0.5$ and 0.127 (of diminished center-shift according to Hongzhe and Shusheng (2010a)) for $\alpha = \pi/4$, as shown in Fig. 7. They are, from now on, named as prototypes 1 and 2, respectively. A four-strip arrangement was employed (two stripes for leaf-spring) to enable the symmetrical placement of the corner cube reflectors used for the measurement of the center-shift components. Each strip was manufactured with 0.5 mm × 10 mm × 60 mm ($T \times W \times L$) resulting in a leaf-spring equivalent width of 20 mm. In order to minimize the shearing effect, a ratio $L/T >> 1$ was adopted. The leaf-springs were made of 0.5-mm-thick sheets of cold rolled austenitic steel (EN 1.4310 FC) with the following mechanical properties: $E = 200\,\text{GPa}$, $\sigma_{0.2} = 1200\,\text{MPa}$ and $S_U = 1350\,\text{MPa}$ – Young's modulus, yield and ultimate strengths. This material was chosen due to its high figure of merit ($\sigma_{0.2}/E$) which avoids plastic deformations in case of accidental loads. To prevent sheet warping owing to machining-induced residual stress, laser cutting was employed to obtain the profiles of the leaf-springs. A sandwich-like configuration was used to assure the effective leaf-spring length. For this purpose, sharp-edge blocks made of martensitic steel were used. They were machined together to avoid assembly misalignments resulting from machining uncertainties. Furthermore, following the approach applied by Zelenika and Bona (2002) mounting jigs were used to guarantee equality of the effective length for both leaf-springs and to avoid twisting while assembling. Moving and fixed members were milled in high strength aluminium blocks, in order to fulfill both: enough robustness to be assumed rigid and low density to reduce the mass required to perform the self-weight compensation.

4.2. Test bench

In order to measure the moving member angular displacements, the optical setup schematically shown in Fig. 8(a) was used. Thus, to perform the measurements, a laser beam emitted by a

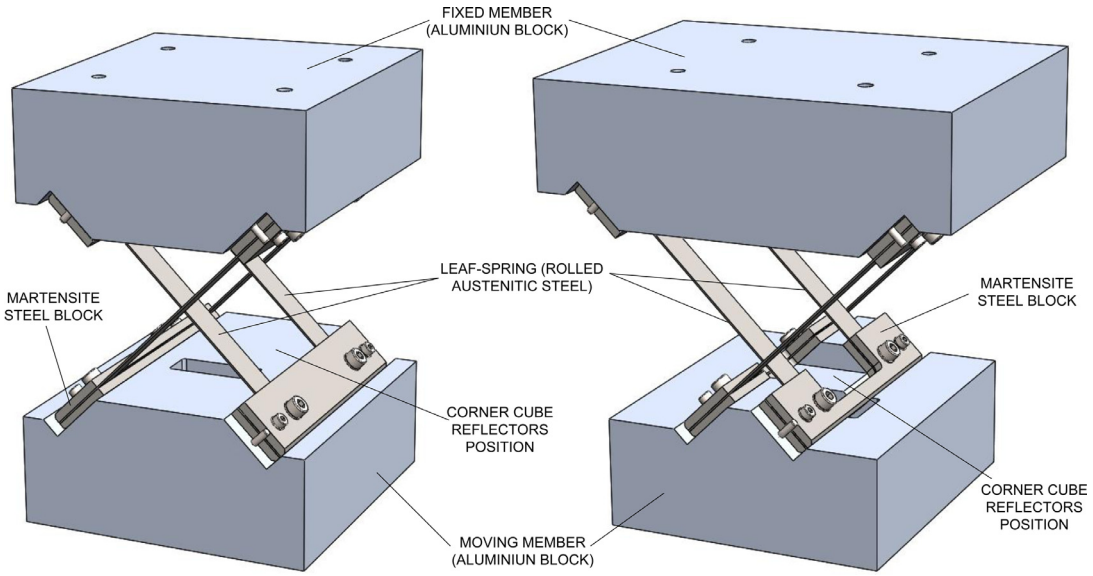

Fig. 7. Cross-spring pivot geometric configurations – (a) prototype 1 and (b) prototype 2.

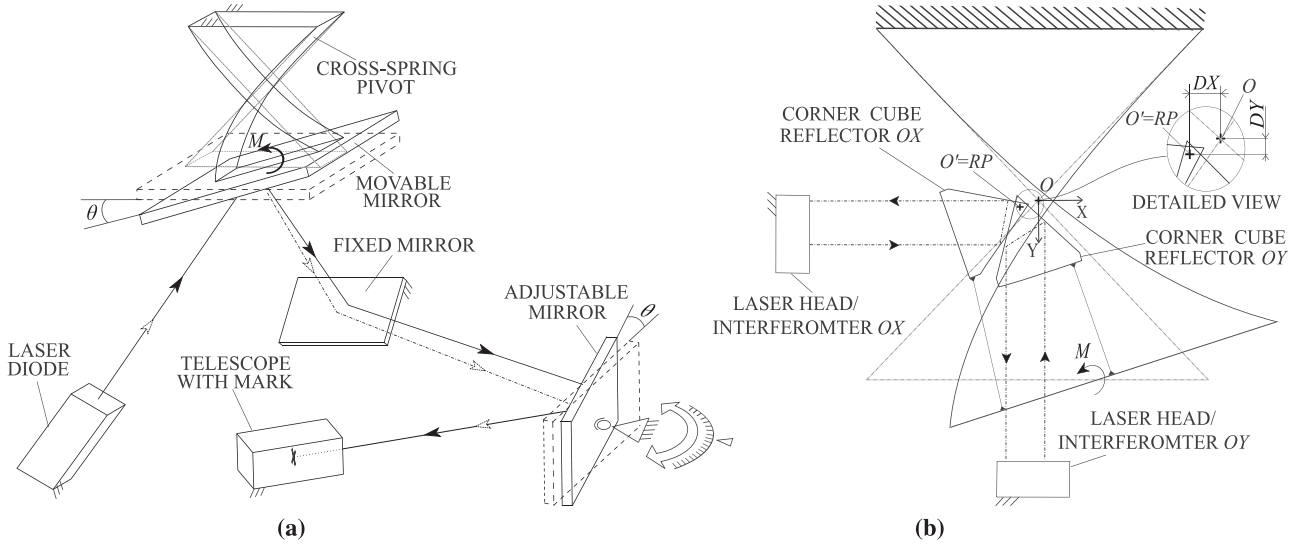

Fig. 8. Schematic representation of the measurement procedures – (a) moving member rotational angle and (b) center-shift.

diode is triply reflected, on a movable, fixed and adjustable mirror, mounted on the pivot moving member, on an aluminium frame and on a rotary table, respectively. This laser beam is then directed toward a telescope with a reference mark inside. The initial angular position of the adjustable mirror is then conveniently set to make the incoming laser match this mark. When the pivot moving member rotates, this beam is deviated outward the mark. Thus, the rotary table is adjusted to realign the incoming beam. The difference between the initial and final angles on the table scale represents the moving member angular shift.

As stated by Zelenika and Bona (2002), the experimental assessment of the center-shift of cross-spring pivots may be performed mapping the trajectory of a single point of the moving member. A few contact and low-resolution non-contact methods using pointers on scribed scale and toolmaker's microscopes were found in the literature for this purpose (Wittrick, 1948; Wuest, 1950; Young, 1944); none of them, however, delivered accurate measurement. On the other hand, the two-dimensional laser tracking technique proposed by Zelenika and Bona (2002) showed to produce reliable results characterized by low uncertainty. Thus, a similar setup was designed to assess the pivot parasitic motion in this work. Nonetheless, on the arrangement applied by them, just one corner cube reflector was used to reflect two in-angle laser beams. Therefore, to determine the center-shift components *DX* and *DY*, this angle must be accurately calibrated and trigonometric expressions have to be applied. To overcome these inconveniences, two laser heads were directed into two independent corner cube reflectors perpendicularly placed to each other on the pivot moving member, as schematically shown in Fig. 8(b). In this case, a fine adjustment of the incoming laser beams was performed by monitoring the output signal in an oscilloscope. Then, the center-shift components were obtained directly by the measurement of each corresponding interferometer.

According to Niebauer et al. (2015), length measurements taken with laser interferometer are invariant to angular movements about the optical center of corner cube reflectors. Thus, an adequate positioning of the corner cubes so that their optical centers coincide with the crossing point of the undeformed leaf-

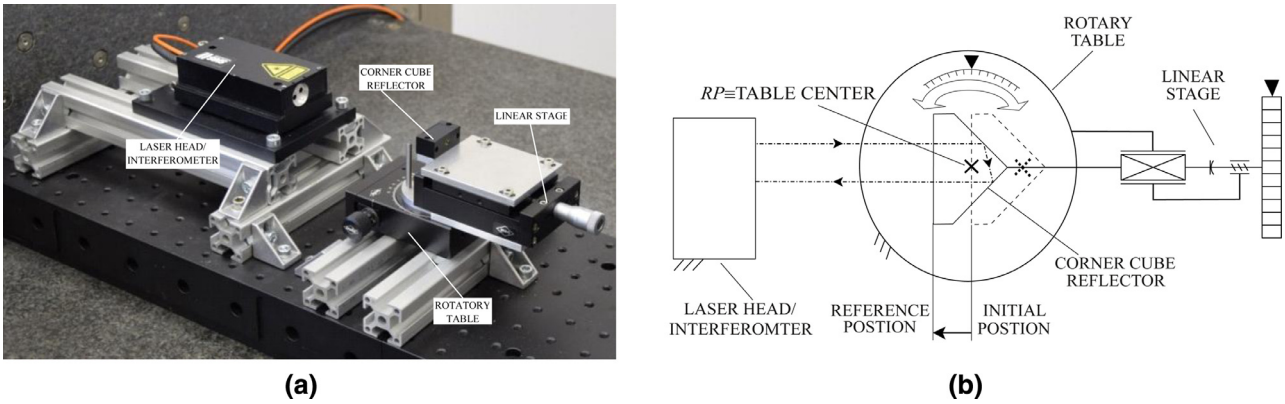

Fig. 9. Measurement of the optical path error due to the corner cubes rotation – (a) experimental setup, (b) schematic representation of the experimental procedure.

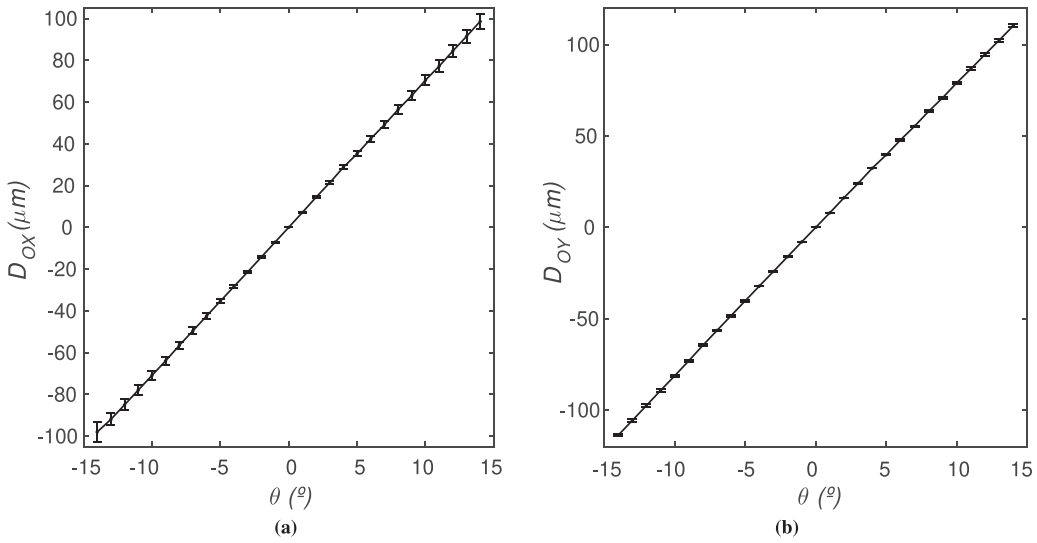

Fig. 10. Compensation curves of the optical path error due to the rotation of the corner cubes – (a) *OX* and (b) *OY*.

springs would eliminate the parasitic displacements accounted on the center-shift measurements, due to the rotation of them. Preliminary experiments showed, however, that the optical center of corner cubes varies from one to another; therefore, locating them accurately becomes a complex task. For this reason, the optical path error resulting from rotations of each corner cube was measured for a reference point (*RP*) instead. To perform the measurement, each corner cube was positioned on a precision linear stage (setting sensitivity of ± 1 µm) that was attached to a graded rotary table (setting sensitivity smaller than 100 µrad), as shown in Fig. 9(a). The interferometer beam was then directed to the corresponding corner cube. Subsequently, this corner cube was carried to the reference position associated to *RP* through a displacement imposed in the linear stage. Finally, rotational increments of 1° were applied to the rotary table and the corresponding displacements where measured by the interferometer (Fig. 9(b)).

Fig. 10 shows the dependence of the optical path error on the rotation of corner cube reflectors *OX* and *OY* (Fig. 8(b)) for a reference position of 6.6 mm from the initial position. Thus, the compensation displacements D_{OX} and D_{OY} were applied to the measurement of the corresponding center-shift components.

Together with the moving member rotational angle and center-shift measurement systems, following the approach employed by Wittrick (1948), resistance strain gauges (S.G.) with thermal expansion coefficient appropriate for austenitic steel ($26x10^6$/K) were fixed on specific points of the leaf-springs to check the stress distribution along their length (shown in the detail of Fig. 11).

The rotary table used in the experiments provides a resolution of 291 µrad (1') through the interpolation of the scale interval (582 µrad). Major source of errors in the measurements of the moving member rotation came up from the laser beam alignment, realignment and reading errors of the rotary table scale. Thus, an uncertainty interval of $\pm$ 873 µrad was estimated for the angular measuring setup. The center-shift measurement system, in turn, provided a resolution of 0.01 µm. The major uncertainties were associated to systematic errors of assembly misalignment, whereas random errors were negligible (refractive index of air, dead-path error, etc (Zelenika and Bona, 2002)). The strain gauge electrical resistances were measured with a resolution of 10 µΩ. Major uncertainties in these measurements arised from parasitic contact resistance. To minimize this effect, an offset compensation feature was set on the data acquisition device (DAQ) used in the stress measurement system (Agilent, 2003).

The pivot prototypes and measurement systems were fixed to the profiled aluminium frame of Fig. 11. The whole test bench was mounted on a vibration isolated granite table, in order to minimize vibration interferences. Couple and vertical loads were applied to the prototypes up to a maximum rotational angle of about 15°. A system of calibrated masses, pulleys and wires tied on the moving member was used for this purpose. Compensation of the moving member self-weight was performed by means of a compressive vertical load (*P* load in Fig. 11). On the other hand, the friction effect was neglected since the frictional moment and force produced by the lubricated rolling-bearings of the pulleys (coefficient of fric-

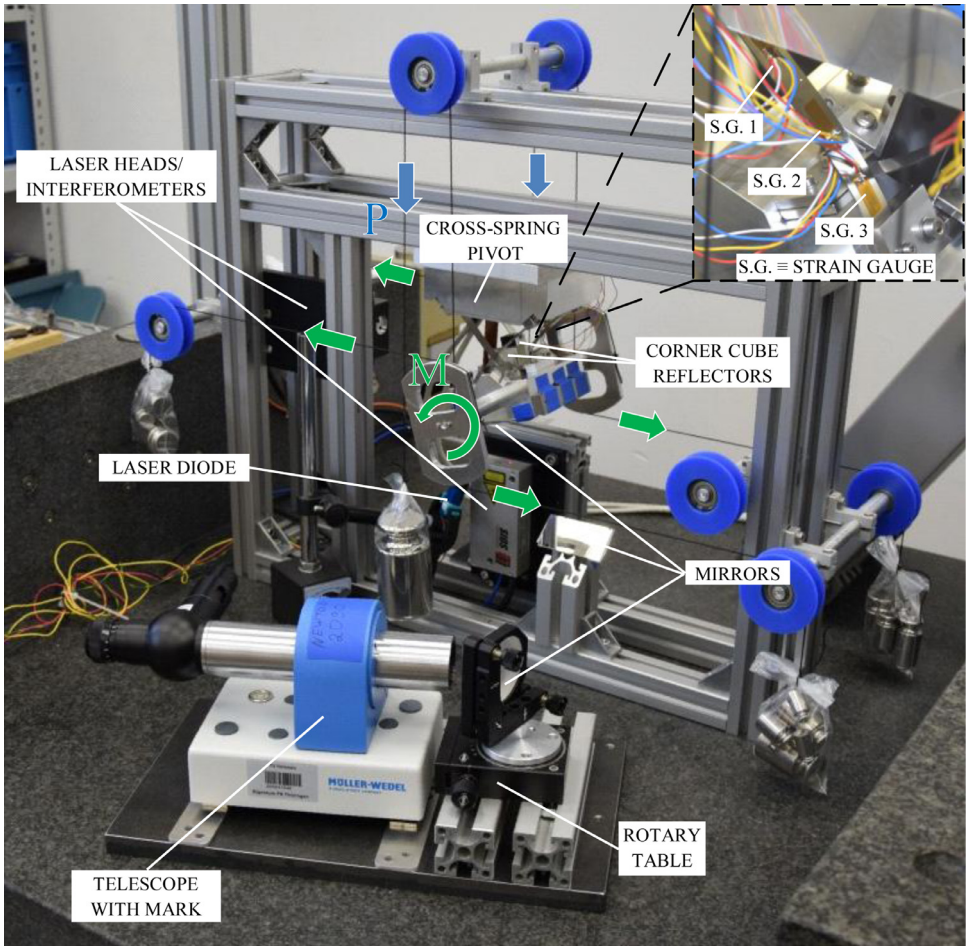

Fig. 11. Experimental setup.

tion $\mu_r \approx 0.001–0.003$) did not overcome 0.012% and 0.006% of the total generated couple and vertical force, respectively. The self-weight of the wires was also neglected.

5. Results and discussion

A comparison between the theoretical results and the experimental measurements performed here and reported in the literature is carried out for both prototypes 1 and 2, in order to check the effectiveness of each model (analytical and FEM) in the prediction of their performance parameters. Furthermore, remarkable design aspects concerning the behavior of the pivot center-shift and rotational stiffness are also discussed.

5.1. Assessment of cross-spring pivots performance parameters

Fig. 12 shows the dependence of the center-shift on the rotational angle θ for prototypes 1 and 2 loaded by pure couple. For the sake of better visualization, the analytical prediction is exhibited on the left axis, whereas the FEM results and experimental measurements are expressed in terms of the difference to the analytical values ($\Delta d = d_{FEM/exp.} - d$) on the right axis.

First of all, there is an excellent correlation between the analytical and FEM results for the prototype 1 (maximum error $|\frac{d_{FEM}-d}{d_{FEM}}| \times 100\% \approx 1.7\%$ for θ around 14.4°). A very good agreement was also achieved when the analytical predictions are compared with the interferometer measurements. The growing difference displayed in this case could be mainly attributed to the approximation in the curvature expression (Zelenika and Bona, 2002). However, the analytical model remains applicable, in even relatively large rotational angles, since an error $|\frac{d_{exp}-d}{d_{exp}}| \times 100\% \approx 6.2\%$ for θ of about 12.8° was obtained. Furthermore, Fig. 12(a) also shows that the measurements provided by the low-resolution non-contact and contact methods (toolmarker's microscopy and pointer on scribed scale) reported in the literatures Wuest (1950) and Young (1944) are characterized by high uncertainties, as revealed by the large differences in even small angular rotations of the pivot moving member.

When the analysis comes to prototype 2, no experimental data was found in the literature. Thus, the analytical results are only compared with the numerical prediction and the interferometer measurements, as shown in Fig. 12(b). Conversely to the accurate results achieved for the prototype 1, a just reasonable correlation between both models was achieved (maximum error smaller than 12.4% for θ of about 11.4°), whereas a large difference occurred when the analytical center-shift prediction and the interferometer measurements are compared. According to Hongzhe and Shusheng (2010a), this pivot configuration ($\lambda = 0.127$ for $\alpha = \pi/4$) produces a diminished center-shift, with X and Y components dominated by high order terms (θ^4 and θ^3, respectively). Thus, the experimental measurements become very sensitive to manufacturing uncertainties and assembly misalignments, which may result in these large differences. Even so, a comparison between interferometer measurements of both prototypes reveals, as expected, that the center-shift of the configuration 2 is substantially smaller

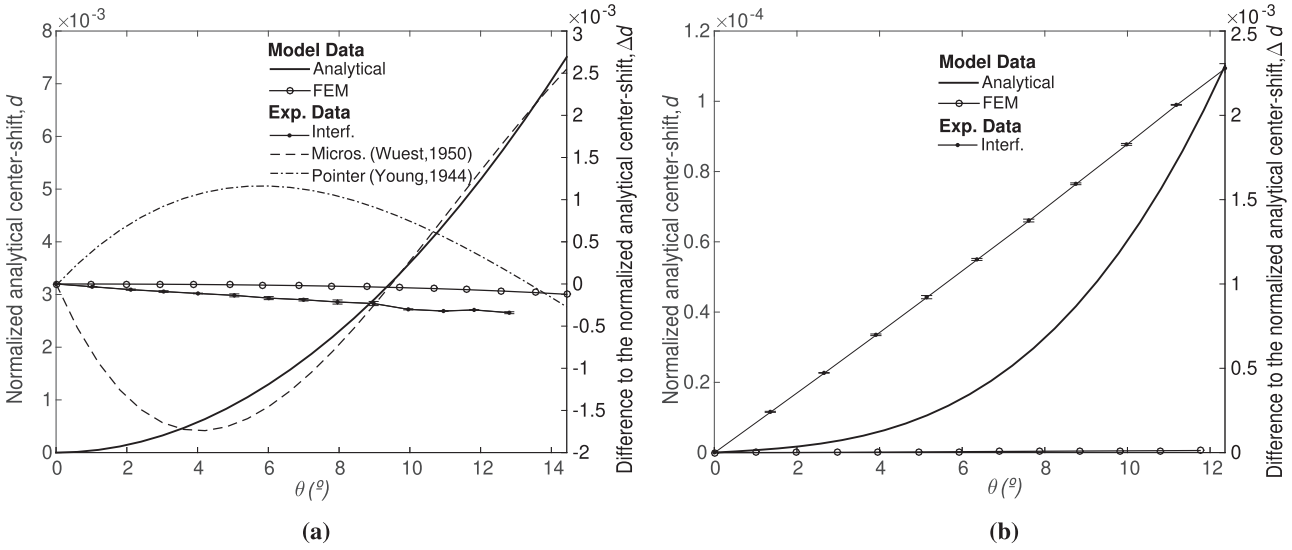

Fig. 12. Normalized analytical center-shift d on the left axis and its difference Δd to FEM and experimental results on the right axis – (a) prototype 1 and (b) prototype 2.

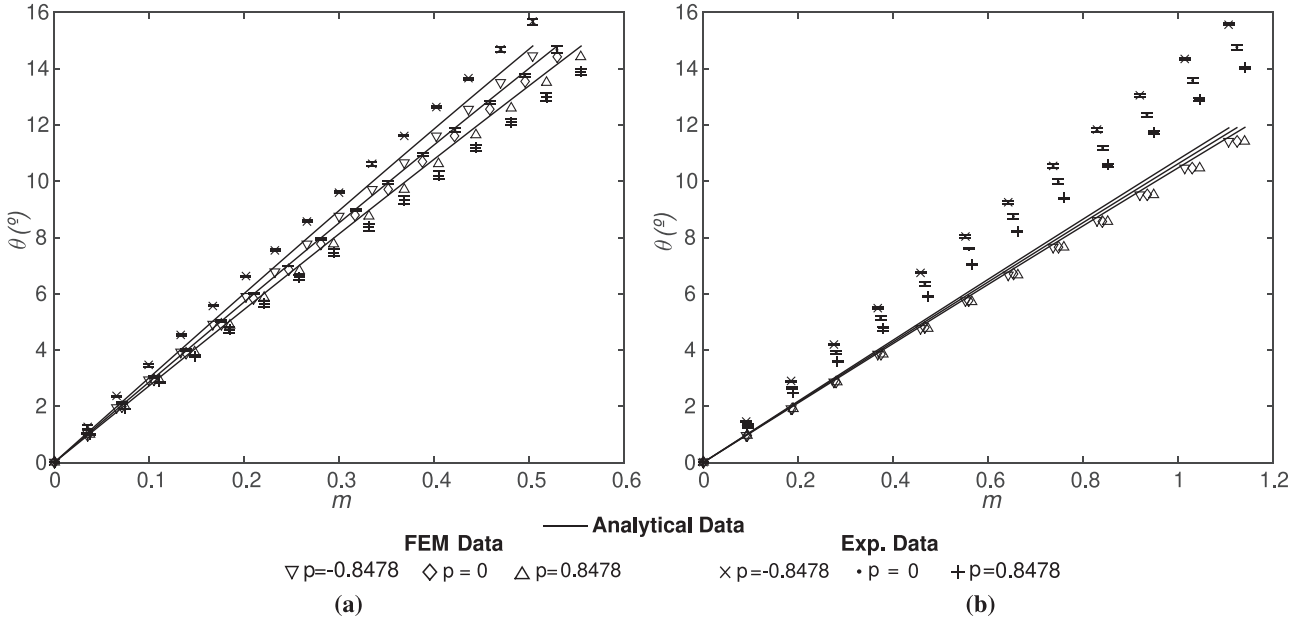

Fig. 13. Stiffness characteristics: normalized couple needed to carry the moving member to a given rotational angle θ (°) – (a) prototype 1 and (b) prototype 2.

than that produced by the prototype 1. Similar results – not shown graphically – were obtained for both prototypes loaded by couple alongside vertical loads (compressive and tensile forces).

Fig. 13(a) and (b) provide a measure of the rotational stiffness of prototypes 1 and 2, respectively. A comparison between them, confirms that a larger couple is needed to carry the moving member of prototype 2 to a certain angular position so that it has a larger rotational stiffness (Gonçalves Jr. et al., 2014). Furthermore, the fairly linear relation between m and θ shown in both cases evidences a constant behavior of the rotational stiffness when the pivot is submitted to pure couple or couple together with a constant vertical load. On the other hand, the stiffness varies when a variable vertical load is considered. In the cases of prototypes 1 and 2, the stiffness decreases under a compressive loading and increases when a tensile force is applied to them. A wider analysis about the influence of the vertical load on the pivot stiffness is presented in the next section.

The results obtained by the analytical and numerical models achieved a very good correlation with a maximum error $|\frac{k_{FEM}-k}{k_{FEM}}| \times 100\%$ of about 2.6% and 4.6% at normalized couples m of 0.55 and 0.74 for prototypes 1 and 2, respectively. The experimental measurements of prototype 1 are in good agreement with both models likewise (error $|\frac{k_{exp}-k}{k_{exp}}| \times 100\% < 10\%$ in most cases), whereas those performed in prototype 2 presented greater errors (maximum in order of 32% when θ is around 1°), which could be due to residual compliance of the constraints (Zelenika and Bona, 2002).

When the stresses are considered, prototype 1 provides a better distribution of compliance along the leaf-springs and due to that, the configuration 2 is submitted to substantially higher stress levels for a given rotational angle θ (critical stress of almost 60% of the material yield strength for a rotational angle of about 14.7°, as shown in Fig. 14(b)). Therefore, this configuration has smaller motion capability than the symmetric one. In addition, measurements of the strain gauges S.G. 2 and S.G. 4 (not shown in Fig. 11),

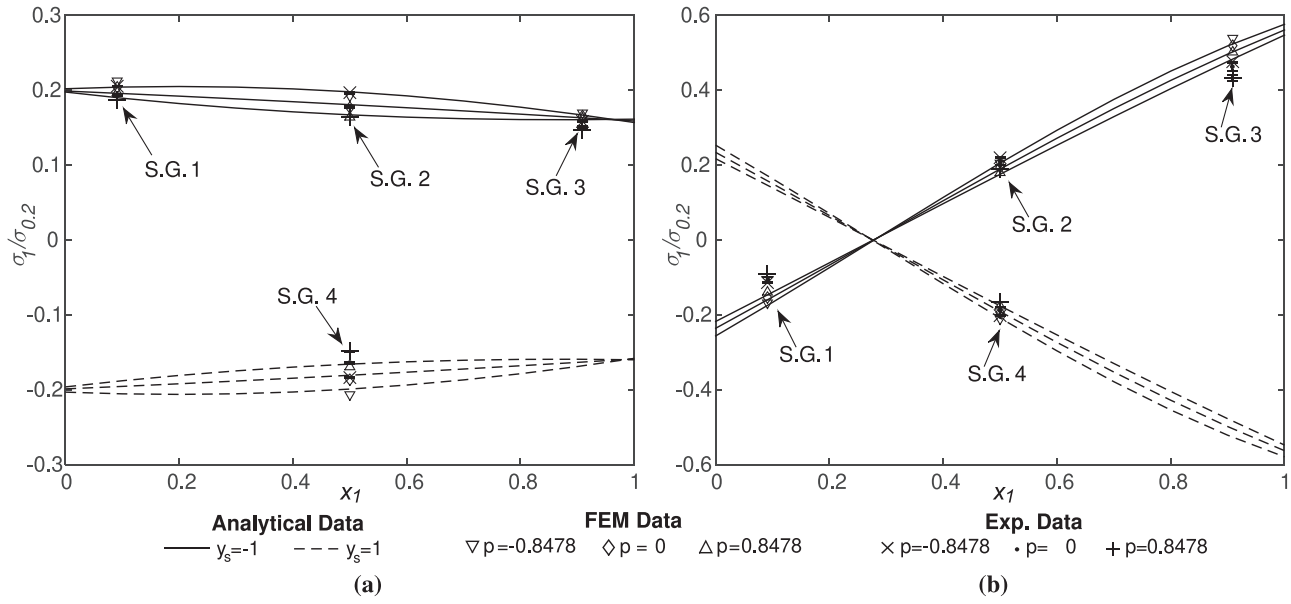

Fig. 14. Stress distribution along the lower ($y_s = -1$) and upper ($y_s = 1$) surfaces of the leaf-spring 1 normalized by the material yield strength – (a) prototype 1 and (b) prototype 2.

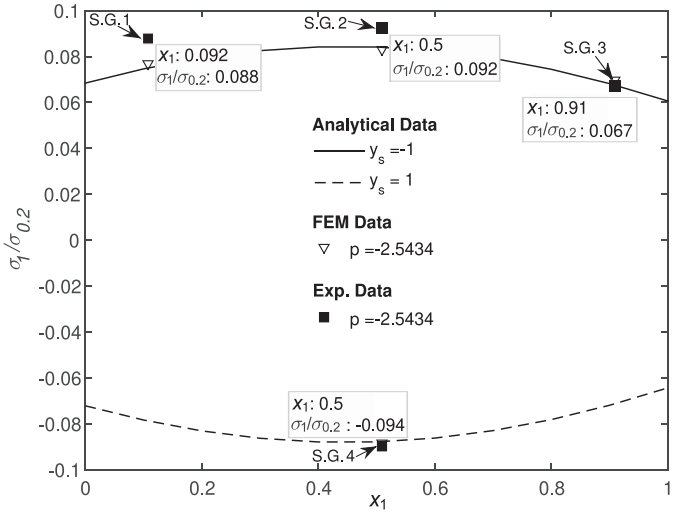

Fig. 15. Stress distribution along the lower ($y_s = -1$) and upper ($y_s = 1$) surfaces of the leaf-spring 1 normalized by the material yield strength for the prototype 1 submitted to a large compressive vertical force.

bonded at opposed faces (y_s=−1 and 1), show that the stress distribution along the leaf-springs is dominated by the bending component, since they produced fairly symmetric values. This conclusion may be extended to a broad angular interval, with the exception of substantially small rotational angles, at which the axial component becomes dominant.

It is also possible to note from Fig. 14 that the critical stress is developed at one end of the leaf-spring. In fact, according to Hongzhe and Shusheng (2010b) it always occurs when the pivot is loaded by pure couple or a couple with tensile load. On the other hand, if a compressive force large enough is applied, the critical stress displaces from the end to an intermediary point of the leaf-spring, as shown by the S.G. 2 and S.G. 4 in Fig. 15.

The comparison among the results provided by the analytical model (normal and dashed lines), finite element analyses (triangle and diamond marks) and experimental measurements (points and cross marks) produced, at least, a reasonable correlation in all cases. Maximum errors ($|\frac{\sigma_{1exp}-\sigma_1}{\sigma_{1exp}}| \times 100\%$) between analytical and experimental data in the measurement of the highest measured stresses did not overcome 3.0% and 12.4% (when θ is about 14.7°) for the prototypes 1 and 2 under the load conditions of Fig. 14 (meas. of S.G. 1 and S.G. 3, respectively). The case of large compressive load, in turn, produced an error smaller than 6.5% for θ around 6.5° (meas. of S.G. 4). A smaller rotational angle was adopted in this case to avoid plastic deformations in the leaf-springs. The errors in the stress measurements could be mainly attributed to the uncertainties associated to the manual process of positioning and bonding the strain gauges.

5.2. Design aspect of cross-spring pivots

The comparison between the theoretical results and experimental measurements performed in the previous section shows that the improved analytical model fulfills the requisites to be applied as a tool to support the design of cross-spring pivots, since the compared results presented a similar global behavior, even though some few did not produce a tight numerical correlation.

When the design of cross-spring pivots is considered, an optimal geometric configuration will depend upon the intended application, since in most cases it is not possible to optimize all performance parameters simultaneously (Marković and Zelenika, 2017). In practice, the geometric parameters λ and α are usually chosen to either optimize the center-shift or the rotational stiffness while a stress check is performed to verify the motion capability of the designed pivot, as well as whether the shape parameters (*T*, *W* and *L*) of the leaf-springs are adequately dimensioned. Thus, the influence of the geometric parameters on the center-shift and rotational stiffness are here analyzed separately and hence conclusions about possible design solutions are drawn.

The center-shift of cross-spring pivots is strongly influenced by their geometric arrangement. Fig. 16(a) shows that this parasitic motion reaches a maximum when λ is 0.5 and increases for large values of α. Moreover, the geometric parameters yield a more pronounced influence on the center-shift in large rotational angles. On the other hand, the pivot geometric configuration presents less impact over this deviation for small rotations ($\theta < 5°$).

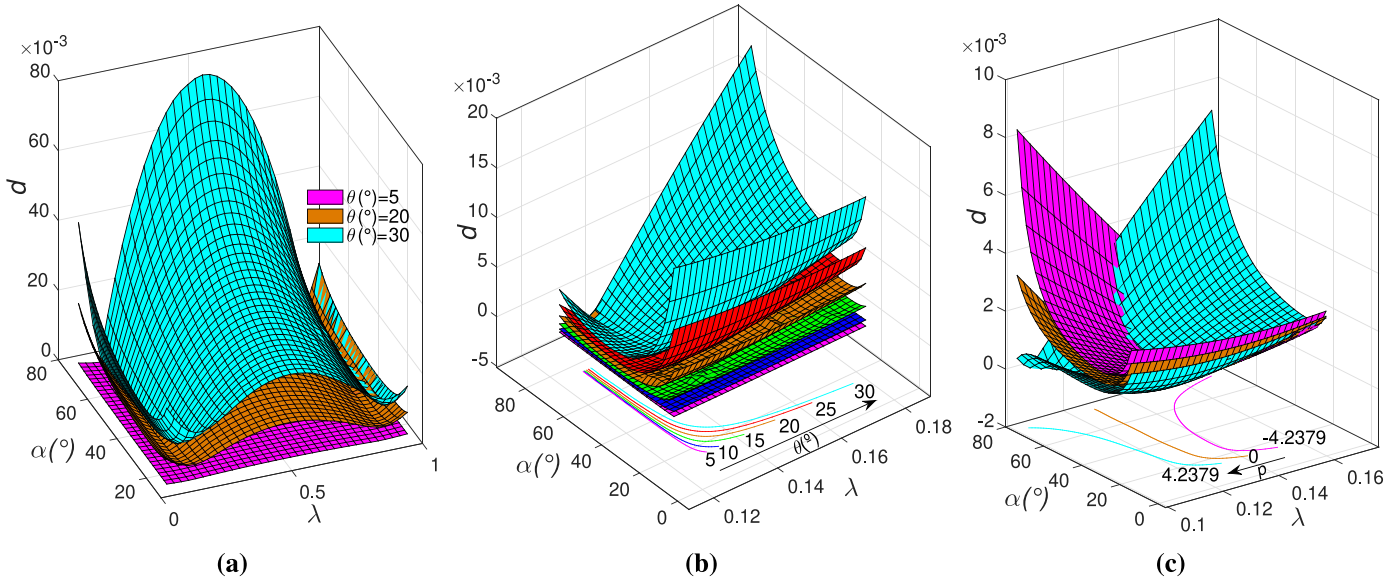

Fig. 16. Influence of the geometric parameters λ and α on the pivot normalized center-shift – (a) for different angles of rotation, (b) diminished center-shift paths for pure couple and (c) diminished center-shift paths for couple combined with the vertical load.

In some specific applications of payload scientific instruments a very small center-shift is required (Henein et al., 2003). According to Marković and Zelenika (2017), the pairs (α, λ) at which this parasitic shift is diminished, varies with the pivot rotation θ. Fig. 16(b) reveals that these values shift toward the symmetric pivot (λ = 0.5) for increasing rotational angles, as shown by the dark arrow. This effect is more pronounced when α becomes smaller than 30° and is accompanied by a substantially increase of the center-shift; on the other hand, the larger α is the smaller the center deviation in this region. A similar behavior is noted for reciprocal pivot configurations (e.g. λ = 0.127 and 0.873).

The coloured curves in Fig. 16(b) represent the projection of the "diminished center-shift paths" for different pivot rotational angles. They show that, when λ < 0.5, 15° ≤α≤ 75° and a range of 5° ≤θ≤ 30° are considered, the center-shift is reduced for λ values varying from 0.1274 up to 0.1760. Analogously, for λ > 0.5 this range varies between 0.8715 and 0.9338 (not shown graphically). These curves are, in both cases, well-fitted by 9th order polynomials as follows:

$$\lambda(\alpha) = a_9\alpha^9 + a_8\alpha^8 + a_7\alpha^7 + a_6\alpha^6 + a_5\alpha^5 + a_4\alpha^4 + a_3\alpha^3 + a_2\alpha^2 + a_1\alpha + a_0. \quad (22)$$

The coefficients a_9, a_8, a_7, a_6, a_5, a_4, a_3, a_2, a_1, a_0 for $\alpha \in [3/36\pi, 15/36\pi]$ of each polynomial are shown in Table 1.

Fig. 16(c) shows, in turn, that the vertical load affects the "diminished center-shift paths" greatly. Thus, when p varies from compressive to tensile loads, the geometric configurations which produce reduced center-shifts change toward the triangular arrangements, i.e. to λ = 0 for pivot configurations in which λ < 0.5 and to λ = 1 for the geometries with λ > 5 (not shown graphically). Furthermore, it is noteworthy a markable variation on the "diminished center-shift paths" for large α values (α > 60°). On the other hand, smaller variations are noted for α varying between 30° and 60°, even when a broad range of p is considered. Owing to that and also to the fact that the center-shift grows substantially for α < 30°, this interval (α ∈ [30°, 60°]) shall be preferred for design matter. The curves for θ = 15°, λ < 0.5 (Fig. 16(c)) and λ > 0.5 (not shown graphically) are well-fitted by 8th order polynomials as follows:

$$\lambda(\alpha) = b_8\alpha^8 + b_7\alpha^7 + b_6\alpha^6 + b_5\alpha^5 + b_4\alpha^4 + b_3\alpha^3 + b_2\alpha^2 + b_1\alpha + b_0. \quad (23)$$

The coefficients b_8, b_7, b_6, b_5, b_4, b_3, b_2, b_1, b_0 for $\alpha \in [3/36\pi, 15/36\pi]$ of each polynomial are shown in Table 2.

Regarding the rotational stiffness, Fig. 17(a) shows that it is strongly influenced by the geometric parameter λ and less sensitive to α variations. Thus, when the pivot is loaded by pure couple, the stiffness minimization is obtained for the symmetric configuration (λ = 0.5) whereas it is maximum for the triangular arrangements (λ = 0 and 1) (Gonçalves Jr. et al., 2014). Similarly, it is possible to see from this figure, that the vertical load p has also a substantial impact on the rotational stiffness behavior.

Table 1
Polynomial coefficients of the diminished center-shift paths for the pivot loaded by pure couple.

	θ(°)	a_9	a_8	a_7	a_6	a_5	a_4	a_3	a_2	a_1	a_0
λ < 0.5	5	−1.011567	7.616263	−25.049645	47.213966	−56.185727	43.781046	−22.353784	7.225946	−1.348271	0.239176
	10	−0.595071	4.789678	−16.827459	33.879746	−43.129231	36.086224	−19.925556	7.045633	−1.461504	0.265137
	15	−4.021361	30.548268	−101.324089	192.502501	−230.821093	181.210051	−93.268360	30.441502	−5.753140	0.613720
	20	−6.568491	49.625305	−163.623492	308.911833	−368.037226	287.168265	−147.024809	47.810507	−9.026126	0.892751
	25	−7.885312	60.393501	−201.989214	387.005671	−468.063230	370.787131	−192.720847	63.616580	−12.193256	1.178165
	30	−10.276802	78.246428	−260.189654	495.814967	−596.816996	471.060437	−244.348190	80.678697	−15.512669	1.473816
λ > 0.5	5	0.663325	−5.198213	17.794030	−34.880942	43.106236	−34.803038	18.359466	−6.112946	1.171664	0.774618
	10	1.682285	−12.913212	43.229113	−82.783721	99.920703	−78.877586	40.797108	−13.382620	2.544431	0.662603
	15	2.177382	−17.256766	59.787865	−118.735443	148.847697	−122.118039	65.610190	−22.311711	4.382229	0.503878
	20	5.411118	−41.530595	139.130793	−266.780651	322.450950	−254.723011	131.618649	−43.010542	8.115843	0.216400
	25	7.452554	−56.742325	188.511207	−358.440185	429.763147	−337.089167	173.234229	−56.443008	10.652945	0.014943
	30	9.303452	−70.777426	235.060327	−447.064450	536.520549	−421.501944	217.081866	−70.898981	13.410464	−0.200183

Table 2
Polynomial coefficients of the diminished center-shift paths for the pivot loaded by couple combined with vertical forces.

	p load	b_8	b_7	b_6	b_5	b_4	b_3	b_2	b_1	b_0
$\lambda < 0.5$	−4.2379	3.348276	−21.658315	60.426156	−94.835550	91.545477	−55.692551	20.910670	−4.453007	0.553547
	0	1.919676	−13.159903	38.723857	−63.839310	64.477440	−40.883114	15.930877	−3.507614	0.466065
	4.2379	1.484218	−10.296389	30.573506	−50.780064	51.626832	−32.949968	12.927825	−2.870914	0.400114
$\lambda > 0.5$	−4.2379	−1.695147	10.643474	−28.891815	44.192930	−41.635469	24.744878	−9.084456	1.890616	0.706353
	0	−1.857842	12.688921	−37.148986	60.845725	−60.967233	38.298721	−14.768157	3.215379	0.580763
	4.2379	−2.570751	17.661291	−51.983096	85.619418	−86.333262	54.639734	−21.252592	4.675435	0.443362

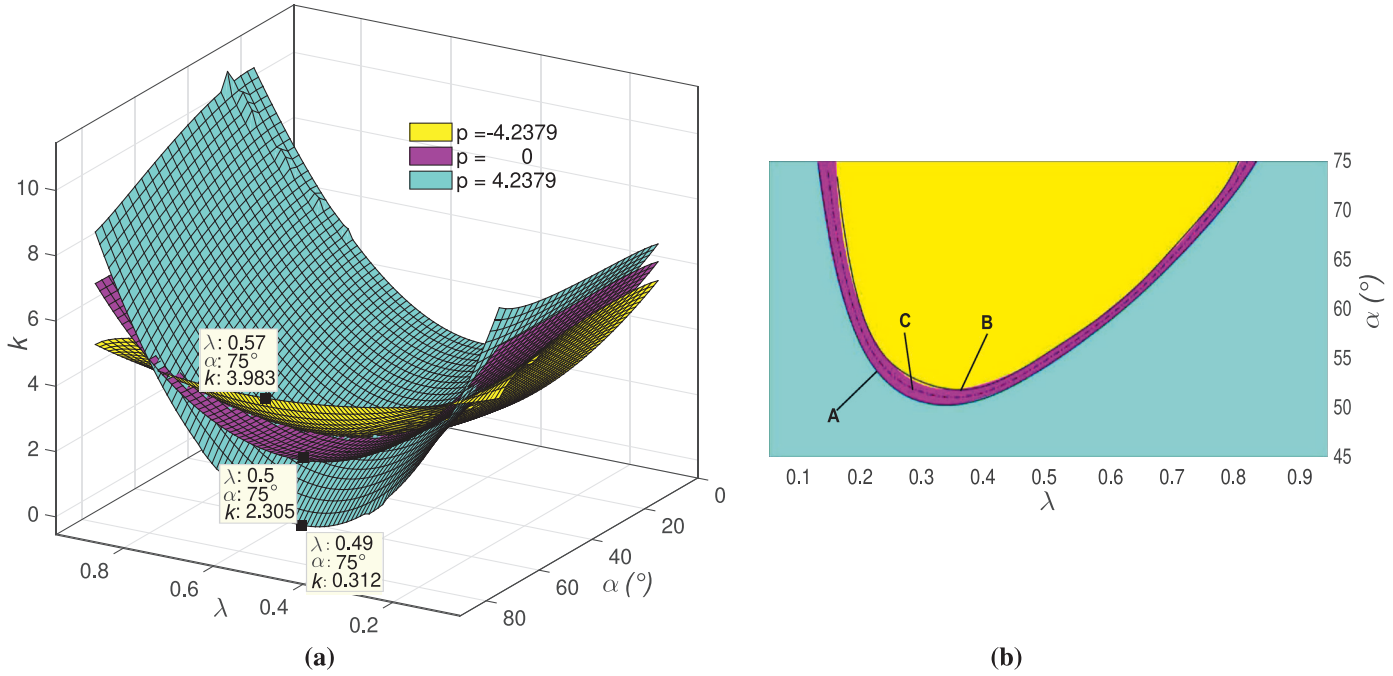

Fig. 17. Influence of the geometric parameters λ and α on the pivot normalized rotational stiffness – (a) for pure couple and couple combined with vertical load, (b) regions delimited by the intercepting curves *A*, *B* and *C* which define different stiffness behaviors under variable vertical loads.

The markers on it show that when the vertical load is positive, the minimum stiffness displaces slightly toward the geometric configuration at which $\lambda = 0$, contrarily for negative p this minimum tends to $\lambda = 1$. This characteristic may be very useful for design purpose since, in general applications, the smaller the pivot rotational stiffness the higher is the instrument sensitivity. However, if it is excessively small, a loss of rotational accuracy may arise, e.g. when a vertical load is applied to the pivot (Bi et al., 2016). Thus, this condition shall be avoided while the pivot is designed.

Fig. 17(b) provides a general picture of the rotational stiffness behavior in dependence of the geometric parameters (λ, α) for a interval of p ranging from negative to positive values. When the pair (λ, α) is selected on the cyan area, compressive and tensile p loads lead, respectively, to a decrease and an increase of the rotational stiffness. On the other hand, the opposite occurs for the yellow region. Thus, for the majority of the geometric configurations, the rotational stiffness is substantially affected by variations of the vertical load. However, in some practical applications, such as torque standard machines (TSM) (Bitencourt et al., 2011; Vasquez, 2014), gimballed devices (Bi et al., 2016), among others, it is desired that the pivot stiffness be invariant to variable vertical loads, in order to reduce realization and measurement uncertainties. According to Hongzhe and Shusheng (2010b), a constant stiffness is obtained if the pair (λ, α) fulfills the following equation:

$$\cos^2\alpha = \frac{-2\left(9\lambda^2 - 9\lambda + 1\right)}{15\lambda}. \tag{24}$$

In fact, it is not possible to design a pivot with constant stiffness, especially when a large range of p varying between positive and negative values is considered (e.g. $p \in [-4.2379, 4.2379]$). Even so, it is still possible to obtain configurations with reduced influence of p variations on the stiffness if λ and α are selected on the transition region in purple. It is important to note that this region is compounded by two subregions: one – delimited by the curves *C* and *A* – defines the selection area of the pair (λ, α) for the particular cases in which the pivot undergoes p variations from 0 over tensile loads, and another – bounded by the curves *C* and *B* – for the cases of p varying from 0 over compressive loads.

Nevertheless, the width of the purple region depends on the limits of p so that the smaller it is, the narrower this region is. For very small magnitudes of it, (e.g. $|p| \leq 0.8476$) the curves *A* and *B* approach the curve *C*, so they become practically coincident and the rotational stiffness quasi-constant (Bi et al., 2016).

The curves *A*, *B* and *C* are well-fitted, for the range of p shown in Fig. 17(a), by the following 9th order polynomials:

$$\alpha(\lambda) = c_9\lambda^9 + c_8\lambda^8 + c_7\lambda^7 + c_6\lambda^6 + c_5\lambda^5 + c_4\lambda^4 + c_3\lambda^3 + c_2\lambda^2 + c_1\lambda + c_0. \tag{25}$$

The coefficients c_9, c_8, c_7, c_6, c_5, c_4, c_3, c_2, c_1, c_0 of each polynomial are written in Table 3.

Where, for *A*: $\lambda \in [0.1287, 0.8342]$, *B*: $\lambda \in [0.1592, 0.8070]$, *C*: $\lambda \in [0.1442, 0.8209]$ and α is given in radians.

Above analyses confirm that it is not possible to obtain a configuration of minimized center-shift and rotational stiffness in once.

Table 3
Polynomial coefficients of the intercepting curves A, B and C that delimit the regions of different stiffness behaviors of the pivot submitted to variable vertical loads.

Curve	c_9	c_8	c_7	c_6	c_5	c_4	c_3	c_2	c_1	c_0
A	−4606.5318	21384.8288	−43085.4068	49393.7105	−35486.7050	16579.6194	−5054.2414	979.2813	−111.5832	6.7240
B	−27560.3189	125460.9055	−248133.9324	279411.4560	−197120.4480	90242.0801	−26794.3356	4981.8084	−528.7167	25.5410
C	−12227.5579	56125.1750	−111809.5812	126689.6560	−89857.2386	41338.3897	−12341.2312	2314.5604	−249.8687	12.9258

However, for practical applications which require high rotational compliance in just small rotational angles (up to 1°) (Bitencourt et al., 2011; Vasquez, 2014), the pair $(\lambda, \alpha) = (0.5, 55.54°)$ – over curve C – may be chosen, since it provides the minimization and also just slightly varied stiffness under p load variations, whereas the center-shift is not significantly disturbed by the geometric configuration for small rotations of the pivot moving member (no problem to select λ=0.5 in this case). For general cases, the polynomials defined by Eqs. (22), (23) and (25) may be used to support the pivot design.

6. Conclusions

In this paper the non-linear effect of the leaf-spring anticlastic curvature was introduced in the analytical formulation proposed in our prior art Gonçalves Jr. et al. (2014) to predict the elasto-kinematic behavior of cross-spring pivots. Furthermore, a non-linear thin shell-based FEM model and an experimental test bench were built to verify the analytical results.

Performance characteristics (i.e. center-shift, rotational stiffness and stress along the leaf-springs) were experimentally assessed for two geometric configurations: $\lambda = 0.5$ and 0.127 for $\alpha = 45°$. The comparison between the results achieved by both models and the experimental measurement showed at least a good agreement for the symmetric configuration ($\lambda = 0.5$). In the case of the asymmetric arrangement ($\lambda = 0.127$), theoretical and experimental data did not produce a tight numerical correlation for the center-shift, possibly due to the high sensitivity of this parasitic motion to manufacturing uncertainties and assembly misalignments of the experimental setup. The rotational stiffness and critical stresses of this configuration presented, in turn, a reasonable and a good agreement, respectively.

Comparison of the analytical results with the numerical and experimental data ensure that the improved analytical model satisfies the requisites to be applied as a design tool of cross-spring pivots. Thus, analyses of design aspects of this type of flexural joint showed that the geometric parameters λ and α affect the pivot performance characteristics significantly. Furthermore, they evidenced that it is usually not possible to obtain an optimal geometry to fulfill a broad range of applications, since the improvement of determined performance parameter leads to a worsening of others, e.g. an optimal center-shift characteristic leads to high rotational stiffness and high critical stresses and vice-versa.

The pivot center-shift is substantially reduced within the intervals of $\lambda \in [0.1274, 0.1760]$ and $\lambda \in [0.8715, 0.9338]$ for $\alpha \in [15°, 75°]$, when a pure couple loading and moving member rotations θ varying from 5° up to 30° are considered (smaller θ values lead to a small impact of the geometric configuration on the center-shift). When a vertical force is applied alongside the pure couple, it is shown that the λ values which produce a diminished center-shift change according to the force direction and magnitude. For a tensile load, λ values move toward the triangular configurations (λ = 0 and 1) and to the symmetric arrangement ($\lambda = 0.5$) for compressive loads.

Contrary to the center-shift, the rotational stiffness reaches a minimum when λ is around 0.5. Furthermore, it is also affected by the variation of the vertical load. However, this effect can be minimized if the pair (λ, α) is adequately chosen. For instance, the geometric configuration of $\lambda = 0.5$ and $\alpha = 55.54°$, provides a high compliance of motion and also a fairly stable stiffness for even broad intervals of variable vertical loads. Due to its good stiffness characteristics, this configuration is suggested for specific applications whose require high "in-plane" compliance in just small angles of rotation, e.g. Torque Standard Machines (TSMs) and gimballed devices.

Acknowledgments

This work was supported by the research project DINTOR/DEBRATOR, a sub-project of the BRAGECRIM research initiative funded by CAPES (Grant no. 018/2012) (Brazilian Research Foundation) and DFG (Grant no. TH 845/5-1) (German Research Foundation). The authors would like to thank Mr. Antônio Carlos Peixoto Bitencourt, Mr. Simon Winter and Mr. Alexander Wagner for the support in the early stages of this work.

Appendix A. Solutions of the approximated curvature expression

To obtain the solutions of Eq. (6), it is integrated twice. In order to determine the constants of integration, the following boundary conditions are employed:

$$\frac{\mathrm{d}}{\mathrm{d}x_i} y_i(0) = 0,\ y_i(0) = 0,$$

Thus, performing the integration of Eq. (6), the slope in dependence of the leaf-spring length is obtained:

$$\frac{\mathrm{d}}{\mathrm{d}x_i} y_i(x_i) = \xi_i f_i \left[\frac{\sinh\left(\sqrt{\xi_i p_i} x_i\right)}{\sqrt{\xi_i p_i}} - \frac{\cosh\left(\sqrt{\xi_i p_i} x_i\right)}{\xi_i p_i} + \frac{1}{\xi_i p_i} \right] + \frac{\xi_i m_i \sinh(\sqrt{\xi_i p_i} x_i)}{\sqrt{\xi_i p_i}} - \delta y_i \sqrt{\xi_i p_i} \sinh\left(\sqrt{\xi_i p_i} x_i\right). \quad \text{(A.1)}$$

Finally, integrating the resulting Eq. (A.1), the transverse deflection along the leaf-spring length is determined:

$$y_i(x_i) = \xi_i f_i \left[\frac{\cosh\left(\sqrt{\xi_i p_i} x_i\right)}{\xi_i p_i} - \frac{\sinh\left(\sqrt{\xi_i p_i} x_i\right)}{(\xi_i p_i)^{(3/2)}} + \frac{x_i}{\xi_i p_i} - \frac{1}{\xi_i p_i} \right] + \xi_i m_i \left[\frac{\cosh\left(\sqrt{\xi_i p_i} x_i\right)}{\xi_i p_i} - \frac{1}{\xi_i p_i} \right] + \delta y_i \left[1 - \cosh\left(\sqrt{\xi_i p_i} x_i\right) \right]. \quad \text{(A.2)}$$

Appendix B. Equations for the non-linear system initial solution

Eqs. (B.1)–(B.8) represent low-order approximations proposed by Hongzhe and Shusheng (2010b) for the variables θ, p_1, p_2, f_1, f_2, m_1, m_2, δy_1 and δy_2, whereas Eq. (B.9) expresses an approximated solution based on series, linear, inverse linear and inverse

quadratic functions for δx_1 and δx_2 (Awtar, 2004). In order to improve the non-linear system convergence, Eqs. (B.1)–(B.9) are used to generate its initial solution.

$$\theta = \frac{15\cos(\alpha)[\lambda f\cos(\alpha)+m]}{[18\lambda^2-18\lambda+15\lambda\cos^2(\alpha)+2]p+120\cos(\alpha)\left(3\lambda^2-3\lambda+1\right)}, \tag{B.1}$$

$$p_1 = \frac{1}{2}\overline{F}_{11} - \frac{1}{20}\left[(1-12\lambda)\overline{F}_{12}+120\cot(\alpha)(1-2\lambda)\right]\theta, \tag{B.2}$$

$$p_2 = \frac{1}{2}\overline{F}_{21} + \frac{1}{20}\left[(1-12\lambda)\overline{F}_{22}+120\cot(\alpha)(1-2\lambda)\right]\theta, \tag{B.3}$$

$$\begin{aligned} f_1 = &-\frac{1}{20}\left[(1-12\lambda)\overline{F}_{11}+120(1-2\lambda)\right]\theta \\ &+\frac{1}{200}\Bigg[(1-12\lambda)^2\overline{F}_{12}+40\cot(\alpha)(108\lambda^2-78\lambda+7) \\ &-\frac{160}{\sin(\alpha)\cos(\alpha)}(9\lambda^2-9\lambda+1)\Bigg]\theta^2, \end{aligned} \tag{B.4}$$

$$\begin{aligned} f_2 = &-\frac{1}{20}\left[(1-12\lambda)\overline{F}_{21}+120(1-2\lambda)\right]\theta \\ &-\frac{1}{200}\Bigg[(1-12\lambda)^2\overline{F}_{22}+40\cot(\alpha)(108\lambda^2-78\lambda+7) \\ &-\frac{160}{\sin(\alpha)\cos(\alpha)}(9\lambda^2-9\lambda+1)\Bigg]\theta^2, \end{aligned} \tag{B.5}$$

$$\begin{aligned} m_1 = &\frac{1}{60}\left[(4-3\lambda)\overline{F}_{11}+120(2-3\lambda)\right]\theta \\ &-\frac{1}{600}\Bigg[(1-12\lambda)(4-3\lambda)\overline{F}_{12}+120\cot(\alpha) \\ &\times(24\lambda^2-29\lambda+6)-\frac{240}{\sin(\alpha)\cos(\alpha)}(9\lambda^2-9\lambda+1)\Bigg]\theta^2, \end{aligned} \tag{B.6}$$

$$\begin{aligned} m_2 = &\frac{1}{60}\left[(4-3\lambda)\overline{F}_{21}+120(2-3\lambda)\right]\theta \\ &+\frac{1}{600}\Bigg[(1-12\lambda)(4-3\lambda)\overline{F}_{22}+120\cot(\alpha) \\ &\times(24\lambda^2-29\lambda+6)-\frac{240}{\sin(\alpha)\cos(\alpha)}(9\lambda^2-9\lambda+1)\Bigg]\theta^2, \end{aligned} \tag{B.7}$$

where:

$$\overline{F}_{11} = \left(\frac{-f}{\sin\alpha}+\frac{p}{\cos\alpha}\right),\ \overline{F}_{12} = \left(\frac{f}{\cos\alpha}+\frac{p}{\sin\alpha}\right),$$
$$\overline{F}_{21} = \left(\frac{f}{\sin\alpha}+\frac{p}{\cos\alpha}\right),\ \overline{F}_{22} = \left(\frac{-f}{\cos\alpha}+\frac{p}{\sin\alpha}\right).$$

$$\delta y_i = -(1-3\lambda)\theta 1^2 + (1-2\lambda)\theta 1^3 \tag{B.8}$$

$$\begin{aligned} \delta x_i = -\Bigg[&\frac{p_i}{s}+\left(-\frac{3}{5}+\frac{1}{700}p_i\right)\delta y_i{}^2+\left(\frac{1}{10}-\frac{1}{700}p_i\right)\theta\delta y_i \\ &+\left(-\frac{1}{15}+\frac{1}{6300}p_i\right)\theta^2\Bigg] \end{aligned} \tag{B.9}$$

References

Agilent, 2003. User's Guide. Publication Number 34970-90003 (order as 34970-90101 manual set).

ANSYS, 2007. Elements Reference. ANSYS Release 11.0.

Awtar, S., 2004. Synthesis and Analysis of Parallel Kinematic XY Flexure Mechanisms Ph.D. thesis. Massachusetts Institute of Technology, Cambridge MA, USA.

Bi, S., Yao, Y., Zhao, S., Yu, J., 2012. Modeling of cross-spring pivots subjected to generalized planar loads. Chin. J. Mech. Eng. 25 (6), 1075–1085. doi:10.3901/CJME.2012.06.1075.

Bi, S., Zhang, S., Zhao, H., 2016. Quasi-constant rotational stiffness characteristic for cross-spring pivots in high precision measurement of unbalance moment. Precis. Eng. 43, 328–334. doi:10.1016/j.precisioneng.2015.08.013.

Bitencourt, A.C.P., Gonçalves Jr., L.A., Wagner, A., Theska, R., Lepikson, H.A., Weingaertner, W.L., 2015. Nonlinear modelling of cross-spring pivots applied in primary torque standard machines. Int. J. Mech. Eng. Autom. 2, 263–269.

Bitencourt, A.C.P., Theska, R., Wagner, A., Lepikson, H.A., Gonçalves Jr., L.A., 2011. A novel approach in the application of flexure bearings in primary torque standard machines. In: Proceedings of the 11th Euspen International Conference.

Brouwer, D., Meijaard, J., Jonker, J., 2013. Large deflection stiffness analysis of parallel prismatic leaf-spring flexures. Precis. Eng. 37 (3), 505–521. doi:10.1016/j.precisioneng.2012.11.008.

Choi, K., Lee, J.J., Kim, M.Y., 2007. Cartwheel flexure-based compliant stage for large displacement driven by a stack-type piezoelectric element. In: Proceedings of the International Conference on Control, Automation and Systems 2007, pp. 2754–2758. doi:10.1109/ICCAS.2007.4406836.

Dearden, J., Grames, C., Orr, J., Jensen, B.D., Magleby, S.P., Howell, L.L., 2018. Cylindrical cross-axis flexural pivots. Precis. Eng. 51, 604–613. doi:10.1016/j.precisioneng.2017.11.001.

Fung, Y.C., Wittrick, W.H., 1955. A boundary layer phenomenon in the large deflexion of thin plates. Q. J. Mech. Appl. Math. 8 (2), 191–210. doi:10.1093/qjmam/8.2.191.

Gómez, J.F., Booker, J.D., Mellor, P.H., 2015. 2D shape optimization of leaf-type crossed flexure pivot springs for minimum stress. Precis. Eng. 42, 6–21. doi:10.1016/j.precisioneng.2015.03.003.

Gonçalves Jr., L.A., 2016. Caracterização experimental do comportamento elastocinemático de mancais flexíveis de lâminas cruzadas Master's thesis. Universidade Federal da Bahia, Salvador, Brazil.

Gonçalves Jr., L.A., Bitencourt, A.C.P., Theska, R., Lepikson, H.A., 2014. Characterization of the elasto-kinematic behavior of generalized cross-spring bearings. In: Proceedings of the 58th International Scientific Colloquium. Ilmenau, Germany.

Haringx, J.A., 1949. The cross-spring pivot as a constructional element. Flow Turbul. Combust. 1 (1), 313–332. doi:10.1007/BF02120338.

Hasselmeier, H., 1951. Das kreuzfedergelenk als lose- und reibungsfreies Lagerelement und die Abwanderung seines Momentan-Zentrums. In: Jenaer Zeiss–Jahrbuch. Jena, Germany, pp. 240–253.

Henein, S., Spanoudakis, P., Droz, S., Myklebust, L.I., Onillon, E., 2003. Flexure pivot for aerospace mechanisms. In: Proceedings of the 10th European Space Mechanisms and Tribology Symposium. San Sebastian, Spain.

Hongzhe, Z., Shusheng, B., 2010a. Accuracy characteristics of the generalized cross-spring pivot. Mech. Mach. Theory 45 (10), 1434–1448. doi:10.1016/j.mechmachtheory.2010.05.004.

Hongzhe, Z., Shusheng, B., 2010b. Stiffness and stress characteristics of the generalized cross-spring pivot. Mech. Mach. Theory 45 (3), 378–391. doi:10.1016/j.mechmachtheory.2009.10.001.

Linß, S., Erbe, T., Theska, R., 2011. The influence of asymmetric flexure hinges on the axis of rotation. In: Proceedings of the 56th International Scientific Colloquium. Ilmenau, Germany.

Linß, S., Schorr, P., Zentner, L., 2017. General design equations for the rotational stiffness, maximal angular deflection and rotational precision of various notch flexure hinges. Mech. Sci. 8 (1), 29–49. doi:10.5194/ms-8-29-2017.

Liu, L., Bi, S., Yang, Q., Wang, Y., 2014. Design and experiment of generalized triple-cross-spring flexure pivots applied to the ultra-precision instruments. Rev. Sci. Instrum. 85 (10), 105102. doi:10.1063/1.4897271.

Lobontiu, N., Garcia, E., 2003. Two-axis flexure hinges with axially-collocated and symmetric notches. Comput. Struct. 81 (13), 1329–1341. doi:10.1016/S0045-7949(03)00056-7.

Marković, K., Zelenika, S., 2017. Optimized cross-spring pivot configurations with minimized parasitic shifts and stiffness variations investigated via nonlinear FEA. Mech. Based Des. Struct. Mach. 45 (3), 380–394. doi:10.1080/15397734.2016.1231614.

Meijaard, J.P., 2011. Refinements of classical beam theory for beams with a large aspect ratio of their cross-sections. In: Proceedings of the IUTAM Symposium on Dynamics Modeling and Interaction Control in Virtual and Real Environments. Dordrecht, Netherlands, pp. 285–292.

Meng, Q., Li, Y., Xu, J., 2014. A novel analytical model for flexure-based proportion compliant mechanisms. Precis. Eng. 38 (3), 449–457. doi:10.1016/j.precisioneng.2013.12.001.

Merriam, E.G., Howell, L.L., 2016. Lattice flexures: geometries for stiffness reduction of blade flexures. Precis. Eng. 45, 160–167. doi:10.1016/j.precisioneng.2016.02.007.

Merriam, E.G., Lund, J.M., Howell, L.L., 2016. Compound joints: behavior and benefits of flexure arrays. Precis. Eng. 45, 79–89. doi:10.1016/j.precisioneng.2016.01.011.

Niebauer, T.M., Constantino, A., Billson, R., Hankla, A., Nelson, P.G., 2015. Balancing a retroreflector to minimize rotation errors using a pendulum and quadrature interferometer. Appl. Opt. 54 (18), 5750–5758. doi:10.1364/AO.54.005750.

Pei, X., Yu, J., Zong, G., Bi, S., 2010. An effective pseudo-rigid-body method for beam-based compliant mechanisms. Precis. Eng. 34 (3), 634–639. doi:10.1016/j.precisioneng.2009.10.001.

Pei, X., Yu, J., Zong, G., Bi, S., Su, H., 2009. The modeling of cartwheel flexural hinges. Mech. Mach. Theory 44 (10), 1900–1909. doi:10.1016/j.mechmachtheory.2009.04.006.

Pomeroy, R., 1968. Axial curvature and residual stress measurement in thin-walled tubes. Int. J. Mech. Sci. 10 (1), 29–34. doi:10.1016/0020-7403(68)90040-4.

Pomeroy, R., 1970. The effect of anticlastic bending on the curvature of beams. Int. J. Solids Struct. 6 (2), 277–285. doi:10.1016/0020-7683(70)90024-7.

Roweis, S., 2018. Levenberg-marquardt optimization. https://cs.nyu.edu/roweis/notes/lm.pdf retrieved on 04.07.2018.

Searle, G.F.C., 1908. Experimental Elasticity. Cambridge University Press, Cambridge, UK.

Tian, Y., Shirinzadeh, B., Zhang, D., 2010. Closed-form compliance equations of filleted V-shaped flexure hinges for compliant mechanism design. Precis. Eng. 34 (3), 408–418. doi:10.1016/j.precisioneng.2009.10.002.

Vasquez, J., 2014. Drehmomentenerzeugungseinrichtung auf Basis bewegter Massen Master's thesis. Technische Universität Ilmenau, Ilmenau, Germany.

Wang, J., Wagoner, R., Matlock, D., Barlat, F., 2005. Anticlastic curvature in draw-bend springback. Int. J. Solids Struct. 42 (5), 1287–1307. doi:10.1016/j.ijsolstr.2004.08.017.

Wittrick, W.H., 1948. The theory of symmetrical crossed flexure pivots. Aust. J. Sci. Res. A Phys. Sci. 1, 121–134. doi:10.1071/PH480121.

Wuest, W., 1950. Blattfedergelenke für meßgeräte. Feinwerktechnik 54, 167–170.

Yong, Y.K., Lu, T.-F., Handley, D.C., 2008. Review of circular flexure hinge design equations and derivation of empirical formulations. Precis. Eng. 32 (2), 63–70. doi:10.1016/j.precisioneng.2007.05.002.

Young, W., 1944. An investigation of the cross-spring pivot. J. Appl. Mech. 11, 113–120.

Zelenika, S., Bona, F.D., 2002. Analytical and experimental characterisation of high-precision flexural pivots subjected to lateral loads. Precis. Eng. 26 (4), 381–388. doi:10.1016/S0141-6359(02)00149-6.